

# Deep Rib Fracture Instance Segmentation and Classification From CT on the RibFrac Challenge

Jiancheng Yang<sup>ID</sup>, Rui Shi, Liang Jin<sup>ID</sup>, Xiaoyang Huang<sup>ID</sup>, Kaiming Kuang, Donglai Wei<sup>ID</sup>, Shixuan Gu<sup>ID</sup>, Jianying Liu<sup>ID</sup>, Pengfei Liu, Zhizhong Chai<sup>ID</sup>, Yongjie Xiao, Hao Chen<sup>ID</sup>, Senior Member, IEEE, Liming Xu, Bang Du, Xiangyi Yan, Hao Tang, Adam Alessio<sup>ID</sup>, Senior Member, IEEE, Gregory Holste<sup>ID</sup>, Jiapeng Zhang<sup>ID</sup>, Xiaoming Wang<sup>ID</sup>, Jianye He, Lixuan Che, Hanspeter Pfister<sup>ID</sup>, Fellow, IEEE, Ming Li, and Bingbing Ni<sup>ID</sup>

**Abstract**—Rib fractures are a common and potentially severe injury that can be challenging and labor-intensive to detect in CT scans. While there have been efforts to address this field, the lack of large-scale annotated datasets and evaluation benchmarks has hindered the development and validation of deep learning algorithms. To address this issue, the RibFrac Challenge was introduced, providing a benchmark dataset of over 5,000 rib fractures from 660 CT scans, with voxel-level instance mask annotations and diagnosis labels for four clinical categories (buckle, nondisplaced, displaced, or segmental). The challenge includes two tracks: a detection (instance segmentation) track evaluated by an FROC-style metric and a classification track evaluated by an F1-style metric. During the MICCAI 2020 challenge period, 243 results were evaluated, and seven teams were invited to participate in the challenge summary. The analysis revealed that several top rib fracture detection solutions achieved performance comparable or even better than human experts. Nevertheless, the current rib fracture classification solutions are hardly clinically applicable, which can be an interesting area in the future. As an active benchmark and research resource, the data and online evaluation of the RibFrac Challenge are available at the challenge website (<https://ribfrac.grand-challenge.org/>). In addition, we further analyzed the impact of two post-challenge advancements—large-scale pretraining and rib segmentation—based on our internal baseline for rib fracture detection. These findings lay a foundation for future research and development in AI-assisted rib fracture diagnosis.

**Index Terms**—Rib fracture, 3D detection, 3D classification, 3D instance segmentation, computed tomography.

Received 29 December 2024; revised 31 March 2025; accepted 21 April 2025. Date of publication 30 April 2025; date of current version 1 August 2025. This work was supported in part by the National Science Foundation of China under Grant U20B200011 and Grant 61976137 and in part by Shanghai Jiao Tong University Medical Engineering Cross Research under Grant YG2021ZD18. Recommended by Associate Editor C. Petitjean. (Jiancheng Yang and Rui Shi contributed equally to this work.) (Corresponding author: Bingbing Ni.)

This work involved human subjects or animals in its research. Approval of all ethical and experimental procedures and protocols was granted by the Ethics Committee of Huadong Hospital affiliated to Fudan University under Approval No. 2019K146.

Please see the Acknowledgment section of this article for the author affiliations.

Digital Object Identifier 10.1109/TMI.2025.3565514

## I. INTRODUCTION

RIB fractures are a common injury that can result from various causes such as falls, trauma, athletic activities, non-accidental injury, or primary bone tumors and metastatic lesions [1], [2], [3], [4], [5]. Internal injuries such as liver or spleen lacerations, mediastinal injury, pneumothorax, hemothorax, flail chest, and pulmonary contusions may also be associated with rib fractures [6]. The severity of trauma can be indicated by the number of fractured ribs, which can result in increased morbidity and mortality rates [7], [8]. Counting the number of rib fractures is important in forensic examinations for determining the degree of disability [9], [10].

Multidetector computed tomography (CT) scanning is a valuable tool for identifying rib fractures with higher accuracy than standard chest radiographs [8], [10], [11]. However, the sheer volume of images generated by CT scans, coupled with the complex shape of each rib and its diagonal course across numerous CT sections, makes interpreting them challenging [12]. This difficulty is compounded in cases of polytraumatized patients, where radiologists are under pressure to rapidly identify life-threatening injuries [11], [13]. As a result, secondary injuries like rib fractures can be overlooked, with studies showing that up to 20.7% of rib fractures may be missed on CT scans [13], [14]. While most of these missed fractures may be minor, their consequences can still be significant for patients, clinicians, and radiologists. Among different types of fractures, buckle fractures are the most frequently missed type of fracture due to their confusing appearance, and nondisplaced fractures can also be missed when they are parallel to the scan plane of the CT images [15], [16]. Diagnosing subtle fractures is a tedious and time-consuming process, requiring the sequential evaluation of a large number of CT slices, rib-by-rib and side-by-side [12]. In cases where missed injuries are a concern, some experts have recommended double-reading whole-body CT scans in high-risk patients [11]. However, this may not always be feasible.

Emerging artificial intelligence (AI) technology has made significant strides in the field of medical services and delivery, particularly in screening [17], [18], [19], [20], [21], diag-

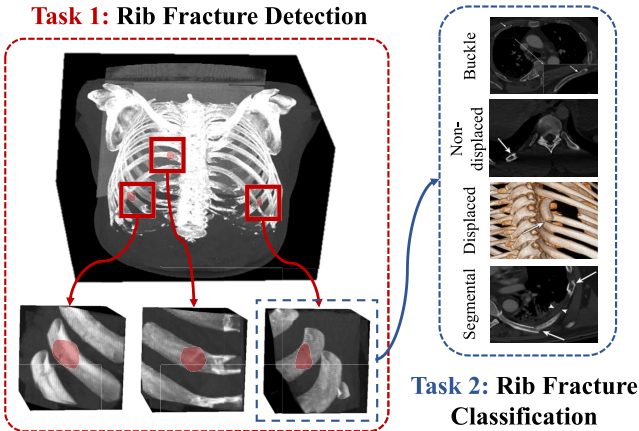


**Fig. 1. Illustration of two tracks in the RibFrac Challenge.** In the rib fracture detection track, participants submit the 3D instance segmentation mask for each fracture to detect their location and extent. In the rib fracture classification track, participants submit the label for each fracture to identify their type (buckle, non-displaced, displaced, or segmental). The red regions are the segmentation masks of rib fracture instances.

nosis [22], [23], [24], [25], [26], [27], and treatment [28], [29], [30], [31], [32]. With high-performance deep learning, computer-aided diagnosis powered by AI can help reduce the burden on human labor, enhance diagnosis consistency and accuracy, personalize patient treatment, and improve the patient-doctor relationship [33]. AI can transform rib fracture diagnosis and treatment by aiding healthcare professionals. Automated diagnosis through AI, such as rib unfolding, streamlines the process and improves accuracy, though training is needed to avoid errors [9], [12], [34], [35]. AI-assisted radiologists, particularly using convolutional neural networks, have shown improved accuracy in rib fracture detection [36], [37], [38]. However, the lack of large-scale annotated datasets and evaluation benchmarks limits deep learning development in this area, underscoring the need for comprehensive datasets and benchmarks for AI model training, evaluation, and research advancement.

The RibFrac Challenge was launched to facilitate the development and evaluation of automated methods for rib fracture detection and diagnosis from CT scans. The challenge provides the first large-scale benchmark dataset of rib fractures from CT scans, comprising over 5,000 rib fractures from 660 CT scans. Each scan has voxel-level instance mask annotations and diagnosis labels for four clinical categories: buckle, nondisplaced, displaced, or segmental. The challenge consists of two tracks: a detection track and a classification track, as illustrated in Fig. 1. In the detection (instance segmentation) track, participants are required to submit the 3D instance segmentation mask for each fracture to detect their location and extent. The detection performance is ranked using a free-response receiver operating characteristic (FROC)-based metric. Segmentation metrics (IoU and Dice) are also provided for analysis, but they are not used for ranking because the rib fracture detection is more important than segmentation in clinical practice. In the classification track, participants are required to submit the label for each fracture to identify their type based on their detection results. The classification performance of the end-to-end system (from detection to classification) is ranked

using an F1 score-based metric. The dataset is the largest publicly available dataset of rib fractures with instance-level annotations, and offers a unique opportunity for researchers to develop and validate deep learning algorithms for rib fracture detection and diagnosis.

The challenge was held as a satellite event during MICCAI 2020, and a total of 243 submissions were evaluated during the official challenge period. From these, seven teams were selected to participate in the challenge summary. The analysis has demonstrated the potential of AI-assisted rib fracture detection and diagnosis, as some of the top detection solutions achieved performance comparable to or even better than human experts. However, the current rib fracture classification solutions are not yet clinically applicable, emphasizing the need for further research and development in this domain. The challenge, both historically and presently, is hosted on the *Grand Challenge* website,<sup>1</sup> offering a comprehensive dataset and an online evaluation platform for advancing research and development in AI-assisted rib fracture detection and diagnosis. As of December 2023, it has attracted over 1,200 registered users. Post the official competition period, additional teams have submitted their results and elevated the benchmark. This indicates that the RibFrac Challenge is actively contributing to the development of deep learning in rib fracture diagnosis.

As an independent technical contribution distinct from the benchmark and challenge, this paper delineates how we have enhanced our internal baseline FracNet [38]. Post the official competition, the field has witnessed significant advancements. For instance, we have developed a point-based rib segmentation technique on the RibFrac dataset [39], [40], which is expected to significantly improve rib fracture detection. Furthermore, the emergence and accessibility of large-scale pre-trained networks for 3D medical imaging have been notable [41]. In light of these developments, we introduced FracNet+, which has achieved competitive results in rib fracture detection. This underscores the beneficial role of rib segmentation in the fracture detection and establishes a foundation for future research in this area.

Our contributions can be summarized as follows:

- **Formalizing research problem.** The RibFrac Challenge represents the first instance of formalizing rib fracture diagnosis as a machine learning problem. The task is well-designed, enabling participants to develop and assess automated methods specifically focused on rib fracture detection and diagnosis.
- **Large in scale.** The dataset stands as the largest publicly available collection of rib fractures with instance-level mask annotations. It comprises over 5,000 rib fractures from 660 CT scans, providing a rich dataset for researchers to train and validate deep learning algorithms.
- **Community impact.** With more than 1,200 registered users, the challenge has garnered considerable interest and participation from the research community. It has been instrumental in the evolution of deep learning algorithms for rib fracture detection and diagnosis.

<sup>1</sup><https://ribfrac.grand-challenge.org/>

- Analysis of post-challenge advancements.** Capitalizing on recent post-challenge advancements in large-scale pre-trained medical models and domain-specific progress in rib segmentation, we analyze their impact by extending our previous internal method for rib fracture detection.

## II. RELATED WORK

### A. Rib Fracture Detection

Several recent studies have explored deep learning approaches for rib fracture detection. For instance, a UNet model incorporating a dual-attention mechanism demonstrated improved performance compared to earlier methods [42]. However, it had limited applicability as it only worked on a restricted number of CT slices. Classic models like DenseNet [43] and ResNet [44] have also been utilized for automatic rib fracture detection [36], [45], but the datasets and models were not released. Some architectures typically used in object detection and image classification, such as CenterNet [46] and DLA34 [47], have been applied to screening and false-positive elimination in rib fracture detection, but they did not include a large validation set [48]. Other studies have focused on the clinical validation of deep learning methods for rib fracture detection. For example, comparative studies have demonstrated that deep learning-based software can be integrated into radiology workflows to enhance rib fracture detection accuracy and reading efficiency [49], [50], [51]. Additionally, [52] utilized a deep convolutional neural network-based software and compared its rib fracture diagnostic performance with doctors, while [53] evaluated the clinical effectiveness of deep learning for rib fractures in trauma patients.

In terms of data scales, [45] includes 1,707 samples with 8,271 fracture annotations, [42] has 818 cases with 3,134 annotations, [52] includes 39 cases with 256 annotations, and [36] contains 56 cases with 199 annotations. However, none of these datasets have been made publicly available. RibFrac is the first and currently the only open-source dataset for rib fracture detection from CT scans. While these prior efforts demonstrate the potential of deep learning-based approaches for rib fracture detection, they also highlight the need for open and large datasets with detailed annotations to improve accuracy and clinical applicability.

### B. Rib Segmentation and Centerline Extraction

Rib segmentation and anatomical centerline extraction play crucial roles in various clinical applications. Rib segmentation provides a stable reference for lung volume estimation [54] and bone abnormality quantification [55]. Anatomical centerlines derived from rib structures enable the localization of organs for surgery planning [56] and the registration of pathologies like lung nodules [57]. Furthermore, automatic rib segmentation and centerline extraction are essential for developing visualization tools for unfolded rib cages [12], [58], [59].

In recent years, several studies have investigated rib segmentation and centerline extraction methods using CT scans. The RibSeg dataset [39], [40] was specifically created to benchmark rib labeling and anatomical centerline extraction

TABLE I

**RIBFRAC DATASET SUBSETS AND FRACTURE CATEGORIES.** THE TABLE SHOWS THE NUMBER OF PATIENTS AND RIB FRACTURES IN EACH SUBSET OF THE RIBFRAC DATASET. THE RIBFRAC CONTAINS FOUR DIFFERENT CATEGORIES OF RIB FRACTURES, INCLUDING BUCKLE (BK), NON-DISPLACED (ND), DISPLACED (DP), AND SEGMENTAL (SG). FRACTURES MISSING CLASSIFICATION LABELS ARE LABELED AS UNKNOWN (UN) AND ARE EXCLUDED FROM THE EVALUATION FOR CLASSIFICATION

Subset	Patients	Fractures	BK	ND	DP	SG	UN
Training	420	3,987	618	567	291	179	2,332
Validation	80	435	69	63	30	30	243
Test	160	882	151	188	84	50	409
Total	660	5,304	838	818	405	259	2,984

using CT scans from the RibFrac challenge. MDUNet [60] employs multiscale feature fusion and dense connections [43] to segment clavicles and ribs. Other approaches include a detection-then-segmentation pipeline with nine degrees-of-freedom pose estimation [61] and trainable segmentation networks that combine multiple 3D UNets at different resolutions [62] for rib segmentation from CT scans. Additionally, studies have focused on rib centerline extraction, employing techniques such as deformable template matching [63] and rib tracing [64] on rib cages detected by deep learning models.

The significance of rib segmentation and centerline extraction could serve as structural references for rib fracture detection. Our internal method has successfully demonstrated its beneficial role.

## III. THE RIBFRAC CHALLENGE

### A. Dataset

1) *Data Acquisition and Pretreatment:* The RibFrac Dataset used in the challenge has been specifically curated for rib fracture detection, segmentation, and classification. This comprehensive dataset consists of chest-abdomen CT scans, rib fracture segmentation, and classification information for a total of 660 unique patients with no duplicates, mean age: 55.1 years (standard deviation 11.82 years; range 21–94 years), with 36.2% of the cohort being female. The data collection was conducted retrospectively and received approval from the ethics committee of Huadong Hospital affiliated to Fudan University (NO.2019K146), with informed consent waived.

To acquire the data, we utilized two advanced CT scanners: a 16 cm wide coverage detector CT (Revolution CT, GE Healthcare, WI, USA) and a second-generation dual-source CT scanner (Somatom Definition Flash, Siemens Healthcare, Forchheim, Germany). Traumatic abdomen-thorax CT scans were performed using the following parameters: 120 kVp, 100–200 mAs, pitch 0.75–1.5, and collimation 1–1.25 mm for both scanners. All imaging data were reconstructed using a bone or medium-sharp reconstruction algorithm with a thickness of 1–1.25 mm. The inclusion of data from two distinct CT scanners could enhance the robustness and adaptability of the developed algorithms. To ensure patient privacy, the CT scans and rib fracture annotations were converted from the raw DICOM (Digital Imaging and Communications in Medicine) to the NIFTI (Neuroimaging

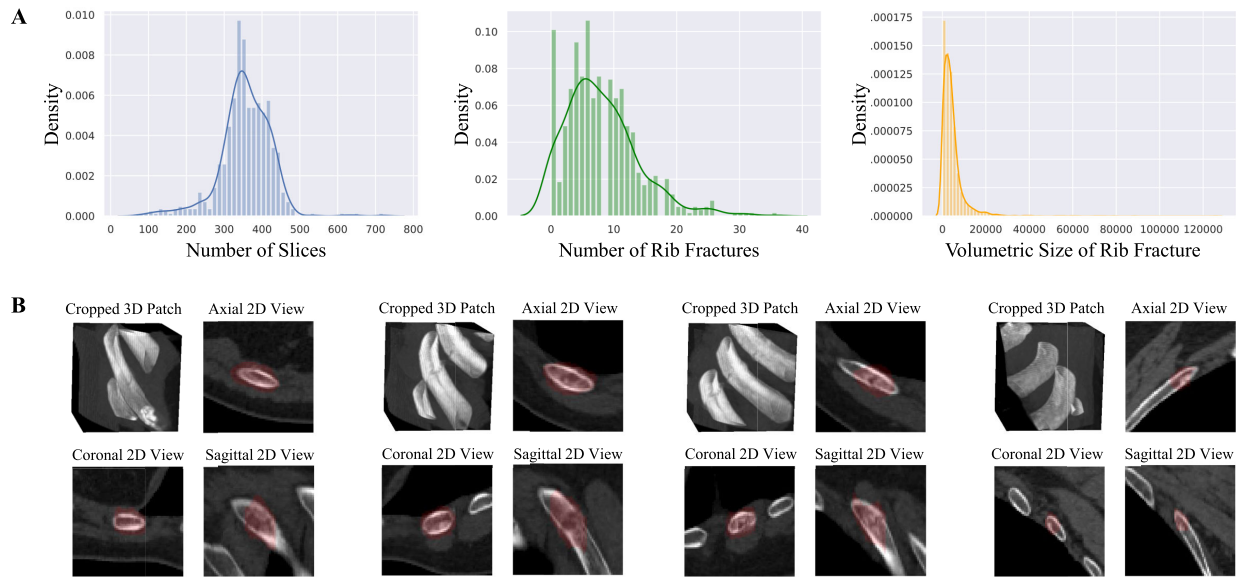


**Fig. 2. Statistics and sample visualization of the RibFrac Challenge dataset. A)** Histograms that display the distribution of the number of slices per scan (left), the number of rib fractures per scan (middle), and the volumetric size of each individual rib fracture (right). **B)** Visualization of four rib fracture samples. Each of the four rib fracture samples is represented by a cropped 3D CT patch using volumetric rendering (upper left). The axial (upper right), coronal (lower left) and sagittal (lower right) from the fracture centroid are shown in 2D, along with the human-annotated rib fracture voxel-level segmentation.

Informatics Technology Initiative) format. We partitioned the dataset into three subsets: the training set (420 samples), the validation set (80 samples), and the test set (160 samples), where the labels for the test set were hidden for evaluation. For a detailed breakdown of the number of patients, CT slices, and rib fractures in each subset, please refer to Tab. I. Additionally, you can find a visual representation of the RibFrac Dataset in Fig. 2, showcasing dataset statistics and sample visualizations.

**2) Data Labeling:** To ensure a fair evaluation in the RibFrac Challenge, five radiologists, labeled as A (5 years of experience), B (15 years), C (5 years), D (5 years), and E (20 years), participated in the labeling process. Initially, radiologists A and B examined the CT images within 48 hours of the examinations. Subsequently, radiologists C and D manually annotated and only annotated the volume of interest for rib fractures based on the diagnosis reports compiled by A and B. The voxel annotations were performed using the 3D Slicer software (version 4.8.1, Brigham and Women's Hospital). The annotations from C and D were later verified by senior radiologist E. When two annotators worked on the same task, they operated on the same workstation and alternated tasks, resulting in an approximate 50-50% split. This study only includes annotations visible to experts from a single scan.

To enhance the comprehensiveness of the annotations, we developed a sophisticated human-in-the-loop procedure that combined the assistance of a deep learning model and human expertise. A deep learning model, following the approach in [38], was trained using the initial training subset of the RibFrac dataset. This model predicted potential fracture region candidates. Predictions that were not covered by the initial labels were verified by radiologist E and added to the annotations if confirmed. Our estimation suggests that approximately 20% rib fractures were missed during the initial labeling. It is important to note that no data leakage issue occurred in the human-in-the-loop labeling process.

In addition to the rib fracture segmentation masks, we also provide classification labels. Rib fractures are classified into four different classes (refer to Fig. 1 for visual examples):

- **Buckle fractures (BK)** are incomplete fractures that appear as bulges in the rib. While buckle fractures are common in pediatric patients across various bones, they can be easily missed in radiology examinations.
- **Non-displaced fractures (ND)** are fractures that do not cause any displacement or misalignment of the bones. Therefore, they can be challenging to identify in radiography. Non-displaced rib fractures may only be observed in follow-up exams when signs of healing have already manifested. Radiologists should be vigilant for associated injuries when there are no direct signs of such fractures in radiography.
- **Displaced fractures (DP)** are those when there are cortical disruptions and significant abnormalities in alignment. Injuries to the surrounding tissues and structures may occur, and several lethal complications related to displaced rib fractures have been documented.
- **Segmental fractures (SG)** are severe injuries characterized by at least two separate complete fractures in the same rib. Those affecting three or more contiguous rib levels are associated with an increased risk of flail chest. SG fractures are labeled as a single mask representing the entire displaced bone section.

Please note that a considerable number of fractures in the dataset are classified as “unknown (UN).” Given the large number of fractures—over 5,000 in total—the annotation workload was immense. This scale partly results from the cohort selection, as the collaborating hospital handles many severe cases. During annotation, physicians were not required to categorize every identified rib fracture. Instead, they were asked to classify up to five of the most clinically

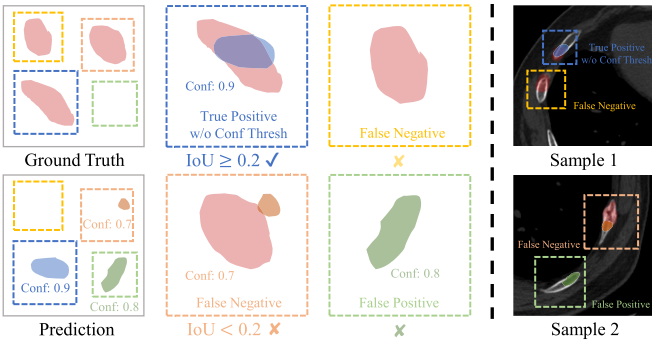


**Fig. 3. Illustration of detection hit in the FROC.** **Left:** A detection proposal is considered a hit (or a true positive without the confidence threshold) when it overlaps with any annotation with an  $\text{IoU} \geq 0.2$  (depicted in blue). The orange and yellow instances represent false negatives, indicating annotated fractures that were not detected. The green one denotes a false positive, indicating a predicted fracture that does not exist. **Right:** Two illustrative samples on CT slices.

significant fractures. Consequently, physicians focused on more prominent or clinically important fractures. Additionally, a human-in-the-loop annotation strategy was employed, where an initial model trained on preliminary annotations proposed new fracture regions for confirmation. While these additional fractures were validated by physicians, many were not considered clinically significant and thus were not categorized. In short, the “unknown (UN)” label does not necessarily indicate fractures that are difficult to categorize. In many cases, these fractures are trivial to categorize or were not categorized due to their large number or lack of clinical importance.

In this context, we believe the presence of the UN category reflects some systematic bias but does not render the classification task meaningless. Fractures labeled as UN were often omitted because they were deemed clinically insignificant (*e.g.*, very small or indistinct fractures) or because the workload of exhaustive annotation was prohibitive. Nonetheless, evaluating the data that has been classified remains meaningful, and in many cases, data with UN labels can reasonably be excluded. During evaluation, these UN fractures are omitted for classification but kept for detection. **Tab. I** presents the statistics of rib fracture classification labels across the RibFrac training, validation, and test subsets.

### B. Evaluation

There are two tracks in the RibFrac Challenge: the detection (instance segmentation) track and the classification track. In the detection track, participants are required to submit the 3D instance segmentation mask for each fracture, aiming to identify the location and extent of the fractures. In the classification track, participants need to submit the label for each fracture to determine its type based on the detection results. The labels for the training and validation sets are provided to the participants, allowing them to assess the model performance. However, the labels for the test set are withheld, and model performance can only be evaluated by submitting the results to the official website of the Grand Challenge.

To ensure transparency and provide participants with detailed evaluation information, the evaluation code is made available.<sup>2</sup>

**1) Detection:** In this task, participants are given the task of detecting rib fractures from CT scans, and the evaluation is based on Free-Response Receiver Operating Characteristic (FROC) analysis for detection. Essentially, participants are engaged in 3D instance segmentation; however, for a more relevant assessment of the algorithms in terms of their practical applicability in clinical settings, we evaluate their performance using an FROC-style detection metric.

In this paper, the terms “detection” and “instance segmentation” are used interchangeably because, while our task involves aspects of instance segmentation, both the task and the evaluation method deviate from the standard definitions of instance segmentation or detection. Importantly, the task does not fall under standard semantic segmentation either. Semantic segmentation assigns each voxel or pixel to a category without distinguishing between individual instances. In contrast, our task requires identifying the location and extent of each fracture, and participants must split their predictions into separate instances (*e.g.*, 1, 2, 3, 4, 5...) to receive a proper evaluation. This is because the FROC-based evaluation relies on the confidence of detection proposals rather than the overall overlap of binary masks. In this context, the distinction between instance segmentation and semantic segmentation is not directly tied to the presence of overlapping objects. While rib fractures in our dataset do not overlap, they can be spatially close to each other. This does not preclude user predictions from having overlapping proposals. If participants submit two closely positioned proposals, they must separate them manually; otherwise, neither proposal may qualify as a detection hit because neither satisfies the IoU threshold.

Due to the elongated shape of rib fractures, the detection task needs to be approached using instance segmentation. Each rib fracture instance is annotated by radiologists with a voxel-level mask that represents the fracture region. However, due to the inherent ambiguity of the fracture region, the instance masks may contain noise. Therefore, segmentation predictions are primarily used to calculate overlap in the detection metric.

The evaluation of the detection performance utilizes FROC analysis, which balances sensitivity and false positives (FP). **Fig. 3** illustrates how the detection hit is calculated in the FROC analysis. It is important to note that for objects with elongated shapes, the Intersection over Union (IoU) tends to vary. For example, in cases with rounded and elongated shapes, even when predictions closely resemble the ground truth visually, the segmentation metrics (*e.g.*, IoU and Dice) for elongated shapes are significantly lower than those for rounded shapes. Consequently, any detection proposal with an  $\text{IoU} \geq 0.2$  is considered a detection hit. Otherwise, it is marked as a false negative (a fracture on the ground truth that was not detected) or a false positive (a predicted fracture that does not exist in the ground truth). For each detection proposal, there is an associated predictive confidence (Conf). When calculating

<sup>2</sup><https://github.com/M3DV/RibFrac-Challenge>

Pred	GT	BK	DP	NP	SG	FP	UN
BK							
DP							
NP							
SG							
FN							



Prediction Aware F1 score  
(exclude FP and FN)



Target Aware F1 score  
(excludes FP)



Overall F1 Score

**Fig. 4. Illustration of classification confusion matrix and three F1 scores.** Overall F1 score (blue) evaluates the end-to-end classification performance (from detection to classification), target-aware F1 score (orange) evaluates performance on the classification annotations (excluding FP), and prediction-aware F1 score (green) evaluates performance on the classification predictions (excluding FP and FN). FN and FP refer to false negative and false positive predictions in detection.

the FROC curve, for each FP level, a confidence threshold (Conf Thresh) needs to be determined. This threshold is used to distinguish whether a detection hit is a true positive or false negative for the current FP level. Furthermore, our evaluation protocol ensures that if a single detection proposal overlaps with two ground truth masks at  $\text{IoU} \geq 0.2$ , it is only considered a hit for the mask with the higher IoU, while the other is treated as a false negative.

The final detection metric used in the challenge ranking is the average of sensitivities at FP levels of 0.5, 1, 2, 4, and 8. In addition to the FROC analysis, we also calculate the maximum detection sensitivity (Max Sensitivity) and the average false positives per scan (Avg FP). These metrics represent the sensitivity and number of FP without considering the FP level. Although the clinical importance of segmentation is not as critical as detection, we also provide the IoU and Dice score for reference in segmentation predictions.

**2) Classification:** In this task, participants are required to classify the detected rib fractures into 4 clinical classes (BK, ND, DP, and SG) based on the results of Task 1. During evaluation, the classification predictions are organized into a confusion matrix with 5 rows and 6 columns, as shown in Fig. 4. The 5 rows represent the 5 categories of predictions: BK, ND, DP, SG, and FN (false negative of detection), while the 6 columns represent the 6 categories of ground truth: BK, ND, DP, SG, FP (false positive of detection), and UN (unclassified labels that are ignored during evaluation). The evaluation metric for classification is the macro-average F1 score, calculated using the confusion matrix. We compute 3 classification F1 metrics, each measuring different aspects of the classification system:

- **Overall F1** evaluates the overall classification performance, integrating it with the detection system. It is used as the final classification ranking metric.
- **Target Aware F1** evaluates the classification performance based on the classification annotations, excluding all false positives.
- **Prediction Aware F1** evaluates the classification performance based on the classification predictions, excluding all false positives and false negatives.

### C. Challenge Setup

The RibFrac Challenge was held as part of MICCAI 2020, following the MICCAI Challenge guidelines and undergoing a rigorous review process that included two independent reviews and a meta review. The challenge design document is available on Zenodo [65]. The evaluation of participant performance was conducted using the established evaluation methods outlined in Section III-B. The ranking metric for the detection track was the average sensitivity in FROC analysis, while for the classification track, the overall F1 score was used to evaluate the end-to-end system. It is worth noting that although the performance of the classification track partially relied on the detection track, the two tasks were evaluated separately.

The challenge consisted of two phases. In Phase 1, participants were provided with training and validation images along with their corresponding labels. In Phase 2, test images were released, and participants were given a two-week period to submit their solutions. During Phase 2, only the ranking metrics were visible to the participants, which were used to determine the final challenge ranking. Publicly available data is allowed only if clearly documented in the submitted solution. During the official challenge evaluation period, participants were allowed a maximum of 2 submissions per day. After the official challenge, users were permitted to make unrestricted submissions and were provided with access to all available evaluation metrics for analysis.

Cash prizes and invitations to the challenge workshop were awarded to the top 3 teams in each track, resulting in a total of 5 teams (with one team overlapping). Additionally, 10 teams were invited to contribute to this paper, and ultimately 7 valid solutions were received.

Following the official MICCAI challenge period, the RibFrac Challenge continues to serve as an online benchmark. All the evaluation metrics, including those used for ranking as well as additional metrics, remain accessible to participants, facilitating continuous monitoring of new developments and enabling further improvements.

## IV. RIB FRACTURE DETECTION TRACK

### A. Challenge Solutions

The top solutions in the detection track are summarized in Tab. II. Among the six top solutions, three utilize 3D neural networks, two use 2.5D neural networks, and one proposes a hybrid pipeline with a 2D detection network and a 3D segmentation network. These solutions do not use any additional datasets. Most of the solutions do not employ any pretraining models, except for one solution that utilizes the ImageNet pretraining. The best-performing solution designs separate networks for false positive reduction, while another solution removes prediction masks with small areas to reduce false positives. The UNet [68], [69] architecture is widely used as the backbone in these solutions. For data augmentation, most solutions employ random flip or rotation, and some also apply random crop. Training losses include cross-entropy loss, Dice loss, smooth L1 loss, and soft IoU loss. Special

TABLE II

**SOLUTION SUMMARY IN THE RIB FRACTURE DETECTION TRACK.** EACH OF THE SOLUTIONS IS SUMMARIZED IN THE FOLLOWING ASPECTS: THE TYPE OF NEURAL NETWORK (2.5D / 3D / HYBRID), PRETRAINING, FALSE POSITIVE REDUCTION (FPR) / MULTI-STAGE (MS), BACKBONE, INPUT RESOLUTION, DATA AUGMENTATION METHODS, TRAINING LOSS, AND SPECIAL REMARKS

Team	2.5D / 3D	Pretraining	FPR / MS	Backbone	Input Resolution	Data Augmentation	Loss	Remarks
lungseg2020 (DT1)	2.5D	ImageNet	Yes	ResNet50 [44]	800×800×15	Random flip	Same as Mask R-CNN [66] (smooth L1, cross-entropy)	ImageNet pretraining
DCC (DT2)	Hybrid	ImageNet	Yes	ResNet50 [44], ResNet101 [44], HRNet32 [67]	1,024×1,024×3, 128×128×32	Random rotation and flip	Cross-entropy, smooth L1, Dice	ImageNet pretraining, Cascade
FakeDoctor (DT3)	3D	No	Yes	3D ResUNet [68]	256×256×256	Random rotation	Cross-entropy, Dice	Model ensemble
UCIrvine (DT4)	3D	No	No	3D UNet [69]	64×64×64	Random flip, rotation, scaling and transition	Cross-entropy, Dice	Model ensemble
MIDLab (DT5)	3D	No	No	3D ResUNet [68]	192×192×192	None	Cross-entropy, Dice	Model ensemble
CCCCS (DT6)	2.5D	No	No	2D UNet [69]	1,024×1,024	None	Dice	Preconditioning operations to extract the ribs

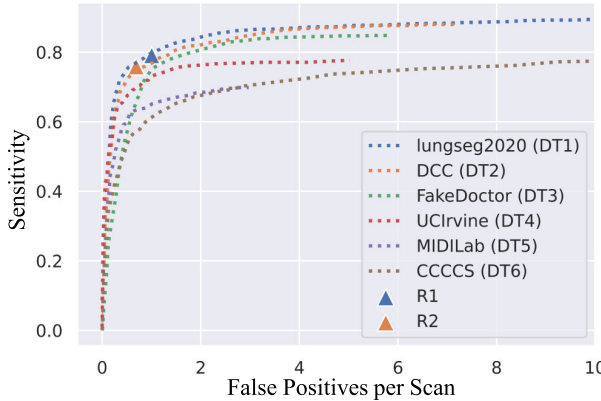


**Fig. 5. Performance comparison between top solutions and human experts.** FROC curves of each solution are displayed in dashed lines, and the performances of human experts are represented in triangles.

techniques such as model ensemble are utilized to improve the detection performance. More method details for each team can be found here [70].

### B. Challenge Results

The results of rib fracture detection for different solutions are presented in Tab. III. Sensitivities at various false positive (FP) levels are reported for each solution, along with their average. The maximum sensitivity and average number of FPs are also provided as additional detection metrics, while Intersection over Union (IoU) and Dice scores serve as segmentation metrics. The average sensitivity at different FP levels is used as the final detection metric for ranking.

DT1 achieved the highest detection FROC score and maximum sensitivity. Among the top solutions, DT5 had the fewest false positives but lower sensitivity. DT3 achieved the highest IoU and Dice scores, indicating superior segmentation performance. However, its FROC score was not as high, indicating possible calibration issues with the confidence of its detection proposals. This suggests that solely optimizing the segmentation network may not be the best strategy for the detection track, considering the low IoU threshold of 0.2 for

detection proposals. It also highlights the effectiveness of false positive reduction.

Fig. 5 illustrates a performance comparison between the top solutions and human experts. In an independent human-only observer study [38], a junior radiologist (R1) and a senior radiologist (R2), both highly experienced in chest interpretation, independently detected and segmented rib fractures in the RibFrac test set. The detection and segmentation metrics were computed based on the ground truth labels. The human experts achieved a detection false positive rate of 1.005 per scan with a sensitivity of 79.1% (R1) and 0.690 per scan with a sensitivity of 75.9% (R2). Despite the human experts having fewer false positives per scan, their detection sensitivities were lower compared to some of the top solutions. When considering the given false positive levels, the top two solutions perform comparably or even better than the human experts.

### C. Discussion

**1) Analysis of Detection TP, FN and FP:** To analyze the relationship between the detection results (TP, FN, and FP), we present the scatter plot of confidence vs. IoU, the confidence histogram of TPs without a confidence threshold, and the histograms of FNs and FPs for each solution in Fig. 6. Interestingly, most solutions demonstrate calibrated confidence values, where the confidence of TPs is generally high, while the confidence of both FNs and FPs is generally low. However, DT3 deviates from this trend, as it shows high confidence values for both TPs and FPs without significant discrimination. This precisely explains why this solution achieved high segmentation metrics but lower detection metrics. This analysis further emphasizes the importance of reducing false positives.

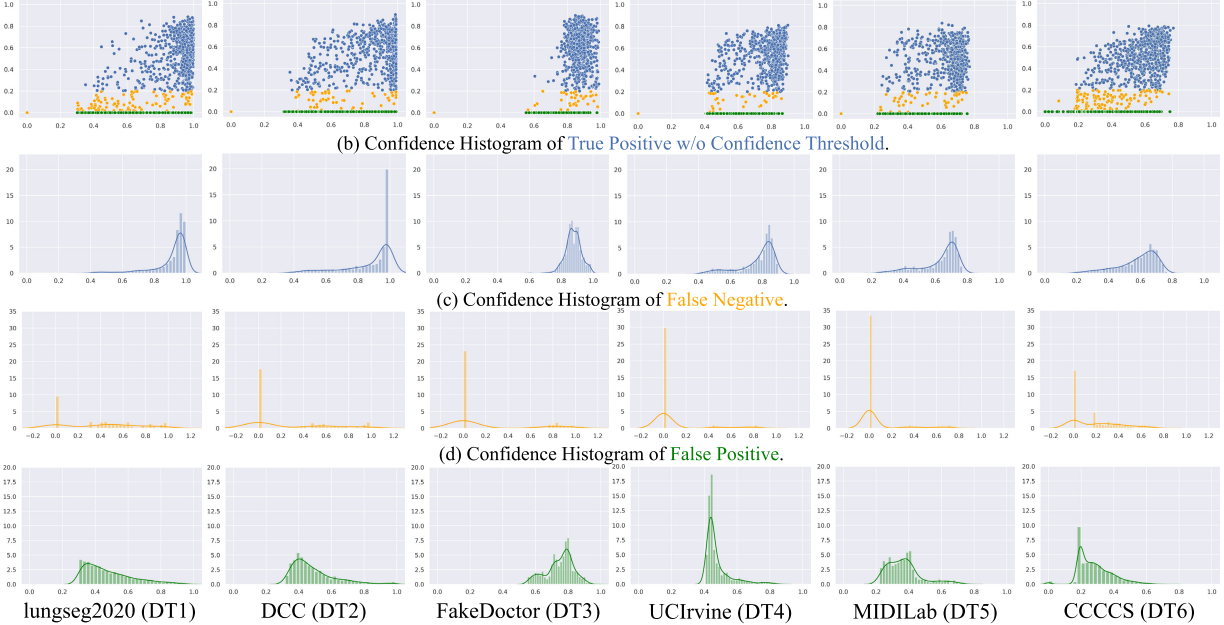
**2) Analysis and Visualization of Segmentation:** We conducted an analysis of the segmentation performance using box plots, as shown in Fig. 7. The plots depict the distribution of IoU values for segmentation, with two variations—one including false positives (FPs) and the other excluding FPs. In the box plot that includes FPs, the segmentation predictions of DT1 and DT6 exhibit low IoU values, indicating a significant presence of false positives in their predictions. This

TABLE III

**A PERFORMANCE COMPARISON OF RIB FRACTURE DETECTION TASK ON THE RIBFRAC TEST SET.** WE REPORT THE FROC METRICS (%), MAX SENSITIVITY (%) AND AVG FALSE POSITIVES FOR RIB FRACTURE DETECTION, IOU (%) AND DICE (%) FOR RIB FRACTURE SEGMENTATION. THE BEST METRICS ARE HIGHLIGHTED IN **BOLD**. THE METRIC FOR RANKING IS HIGHLIGHTED IN BLUE

Method	Detection FROC (Sensitivities @FP levels)						Detection Auxiliary Metrics		Segmentation	
	0.5 ↑	1 ↑	2 ↑	4 ↑	8 ↑	Avg ↑	Max Sensitivity ↑	Avg FP ↓	IoU ↑	Dice ↑
<i>Official Challenge</i>										
lungseg2020 (DT1)	<b>75.06</b>	<b>79.74</b>	<b>84.34</b>	<b>87.06</b>	<b>88.72</b>	<b>82.98</b>	<b>89.80</b>	17.73	44.04	61.15
DCC (DT2)	72.11	76.83	82.10	86.67	87.98	81.14	87.98	7.18	45.86	62.89
FakeDoctor (DT3)	56.74	75.01	80.69	84.36	84.81	76.32	84.81	5.84	<b>47.32</b>	<b>64.24</b>
UCIrvine (DT4)	67.30	73.08	76.30	77.10	77.66	74.29	77.66	5.02	36.52	53.50
MIDLILab (DT5)	60.09	65.01	68.48	69.84	69.84	66.65	69.84	<b>2.97</b>	41.07	58.23
CCCCS (DT6)	53.29	61.19	67.57	72.25	76.00	66.06	80.61	29.10	23.15	37.60
<i>Post-Challenge as of December 2023</i>										
A1	78.92	83.98	85.13	88.44	90.94	85.48	92.91	12.11	42.57	59.71
A2	76.38	83.49	86.90	90.25	91.32	85.67	92.06	12.43	31.23	47.60
A3	69.77	80.68	84.58	84.81	84.81	80.93	84.81	2.37	52.68	69.01

(a) Scatter Plot of Confidence (x) vs. IoU (y). True Positive w/o Confidence Threshold. False Negative. False Positive.



**Fig. 6. Statistics of detection confidence.** The scatter plots (a) illustrate the distribution of detection IoU (y-axis) of each prediction and its corresponding confidence (x-axis). The histograms further display the distribution of confidence score of (b) true positive predictions without confidence threshold, (c) false negative predictions, and (d) false positive predictions of each solution, respectively.

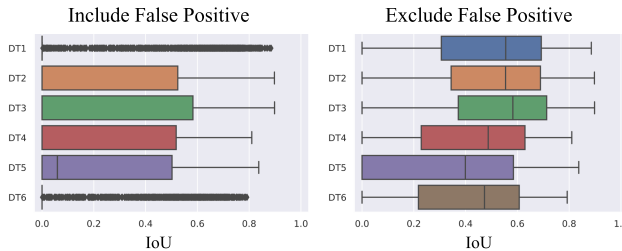


**Fig. 7. Statistics of segmentation performance.** The box plots display the distribution of IoU of segmentation including false positives (left) and excluding false positives (right).

observation is consistent with the average FP metric reported in Tab. III. However, in the plot without FPs, the winning solution achieves high segmentation metrics. This suggests that the team prioritized maximizing sensitivity, which resulted in an increased number of FPs. Nevertheless, they were able to effectively suppress the confidence of these false positives through FPR, leading to a favorable FROC metric in the

ranking, despite seemingly weaker segmentation metrics that were not for ranking.

Furthermore, in Fig. 8, we present a box plot illustrating the distribution of segmentation IoU (disregarding detection FPs) for each category of rib fractures, along with visualizations of predictions for two cases in each category. For each visualization, we selected slices at fixed intervals around the center and annotated the ground truth segmentations in red, while the predictions are represented in blue. The analysis reveals varying levels of difficulty in segmenting different categories of rib fractures. For example, the overall segmentation IoU of buckle fractures is lower compared to that of non-displaced fractures. Contrary to the poor performance indicated in Tab. III, the winning solution demonstrates satisfactory segmentation visualization results when false positives are disregarded.

#### D. Post-Challenge Results

As an ongoing online benchmark, the RibFrac Challenge has received numerous post-challenge submissions, some of which

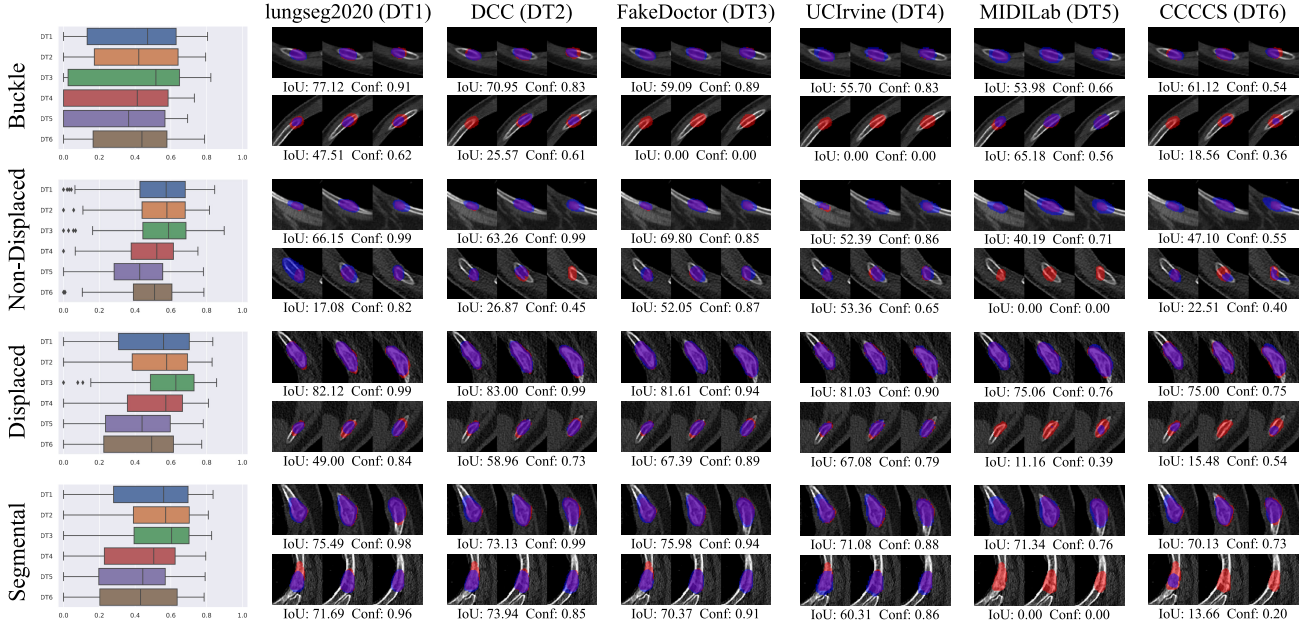


**Fig. 8. Statistics and visualization of segmentation performance for each category of rib fractures.** We provide a box plot showcasing the distribution of segmentation IoU values (excluding detection FPs) for each solution, along with visualizations of predictions for two representative cases. The ground truths are in red, while the predictions are in blue.

are on par with the top solutions during the official challenge period. Three top post-challenge solutions are selected as of December 2023. As participant information is no longer required after the official challenge, we anonymized these submissions as A1, A2, and A3. Among them, the A1 method achieves better sensitivity levels at low FP level ( $FP=0.5$ ), while A2 performs better at moderate FP level ( $FP=4$ ). These advancements demonstrate that the RibFrac Challenge remains active and contributes to the development of methodologies.

On the other hand, we have observed limited progress in rib fracture classification. This is partly due to the inherent difficulty of rib fracture classification itself (as discussed in the analysis in Sec. V-B), and partly because the performance of the classification track in the RibFrac Challenge is heavily influenced by the detection performance, which can be overlooked by participants. We plan to address this issue to some extent in future versions of the RibFrac Challenge by modifying the evaluation methods, with the aim of promoting overall performance in the rib fracture classification task.

## V. RIB FRACTURE CLASSIFICATION TRACK

### A. Challenge Solutions

Tab. IV provides a summary of the top solutions in the classification track. All of the top solutions employ 3D neural networks without pretraining, except for one team that utilizes a 3D ResNet-50 [44] pretrained on Med3D [71]. The input resolutions vary from  $64 \times 64 \times 64$  to  $128 \times 128 \times 64$ . While the top two solutions employ random rotation and flip for data augmentation, the remaining solutions do not utilize any data augmentation methods. Cross-entropy loss is used as the training loss for all teams, with two teams also employing Dice loss as an additional loss function. To enhance classification performance, some teams employ special techniques such as dilated convolution [72], auto-context mechanism [73], and

class-weighted loss. More method details for each team can be found here [70].

### B. Challenge Results

The results of rib fracture classification are presented in Tab. V. We provide the prediction-aware F1 score, target-aware F1 score, and overall F1 score for each rib fracture category, as well as their macro-average. It should be noted that the prediction-aware, target-aware, and overall F1 scores may not be consistent across the solutions, as these three classification metrics are biased towards the detection performance. However, since the labels of the test set are completely hidden, the classification track emphasizes the evaluation of end-to-end systems. The macro-average overall F1 score across the four categories is used for ranking.

Upon examining all the solutions, it is observed that the DP and ND fracture types are relatively easy to distinguish, while the BK type is slightly more challenging. However, the SG type shows very poor discriminative performance. Overall, although these solutions outperform random guessing, unfortunately, they are still far from being clinically applicable, verified by clinical experts, especially for SG classification. In the following sections, we will analyze why the task of rib fracture classification is so challenging.

### C. Discussion: Why the Fracture Classification Is Hard

1) *Diagnostic Challenges and Class Imbalance:* The diagnostic approaches for these four types of fractures vary significantly. Non-displaced fractures (ND) and displaced fractures (DP) both involve complete fractures, with the distinction being the presence or absence of bone displacement or misalignment. As a result, these two types of fractures are relatively conspicuous and can be diagnosed based on their geometric positions. The results indeed indicate a higher diagnostic performance for ND and DP fractures. On the other hand, buckle fractures (BK) are incomplete fractures that

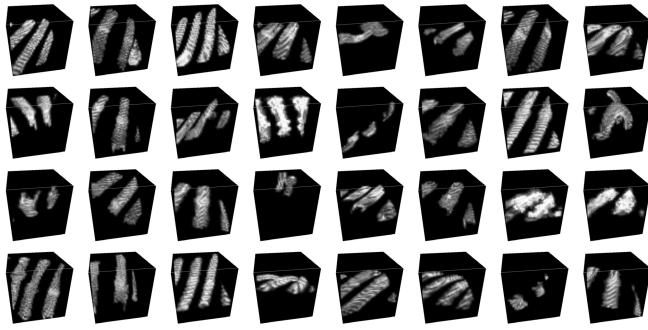


**Fig. 9.** Examples of rib fracture instances. Each sample is center-cropped into a  $64 \times 64 \times 64$  volume.

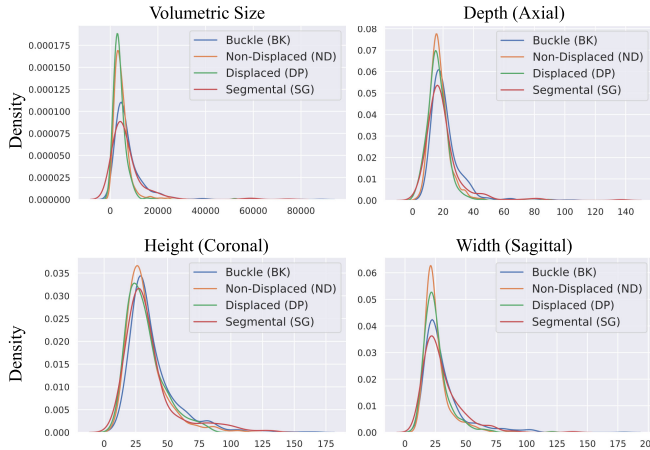


**Fig. 10.** Statistics of sizes for each rib fracture category. The histograms display the distribution of the volumetric size (top left), depth (top right), height (bottom left), and width (bottom right) of each individual rib fracture in each category.

typically manifest as bulges in the rib. This makes them easily missed in radiology examinations, leading to a higher difficulty in diagnosis and an increased number of false negatives in detection. The results demonstrate a significant improvement in the numerical value of the prediction-aware F1 score for BK fractures compared to the target-aware and overall F1 scores, as false negatives are excluded from the prediction-aware calculation. Segmental fractures (SG), in contrast, are defined as severe injuries characterized by at least two separate complete fractures in the same rib. Diagnosing SG fractures solely based on local information is not feasible. However, all the methods in the challenge utilized local patches, which resulted in poor discriminative performance for the SG.

Moreover, due to the RibFrac dataset being collected from real clinical scenarios, there is an imbalance in the distribution of fracture categories (as shown in Table I). This further adds to the difficulty of machine learning tasks.

**2) Geometric Complexity:** Rib fracture classification also faces the challenge of geometric complexity. Fig. 9 showcases several instances of rib fractures, where each sample is center-cropped into a  $64 \times 64 \times 64$  volume. It can be observed that these 3D patches exhibit significant variations in orientation, shape, and appearance, posing a significant challenge for CNNs, which are sensitive to rotation. Despite the ideal assessment of rib fractures based on individual ribs, these 3D patches unavoidably contain multiple ribs, introducing additional background noise.

Furthermore, the sizes of the four fracture categories vary greatly. Fig. 10 illustrates the distribution of volumetric size, depth, height, and width for each rib fracture category. These categories exhibit considerable size variation, and there is significant overlap between them, further complicating the classification task.

**3) Future Directions on Rib Fracture Classification:** To better bridge this gap, future work could explore integrating anatomical context or rib-wise relational modeling into the classification pipeline. Moreover, strategies such as rib-wise aggregation of local features or pretraining on rib parsing tasks may improve classification robustness.

We also emphasize that current classification performance—while modestly promising—is still far from being clinically applicable. As such, we view this task as an open problem and invite further exploration from the research community. By providing a standardized dataset, benchmark, and initial analysis, we hope this work lays the foundation for ongoing community-driven efforts to advance AI-based rib fracture classification.

## VI. ANALYSIS OF POST-CHALLENGE ADVANCEMENTS OF RIB FRACTURE DETECTION: INTERNAL METHOD

In this section, we analyze the impact of two recent post-challenge advancements—point-based rib segmentation and large-scale pretraining for 3D medical imaging—by applying them to a previously developed internal rib fracture detection baseline, FracNet [38]. This analysis aims to provide practical insights into how these techniques may benefit future research on rib fracture detection.

Specifically, we first briefly review the original FracNet approach and then investigate the effect of integrating two representative advances: a point-based rib segmentation technique [39], [40] and a large-scale pre-trained network, STUNet [41], designed for volumetric medical images. We refer to this updated pipeline as FracNet+ for clarity of presentation, and provide an overview in Fig. 11.

It is important to emphasize that this investigation is not intended to propose FracNet+ as a novel or standalone contribution. Rather, it serves as part of a broader analysis to evaluate the RibFrac benchmark and to explore the utility of emerging tools and infrastructure upgrades. Our findings suggest that both rib segmentation and large-scale pretraining are promising directions and may offer practical, out-of-the-box benefits for future studies in this domain.

### A. FracNet as an Internal Baseline

In rib analysis, traditional methods primarily rely on the extraction of rib centerlines, followed by techniques such as rib unfolding [12], [58] to convert original 3D images into 2D stacks for analysis. While this approach effectively utilizes anatomical knowledge of the ribs, it often encounters issues like false negatives due to the limitation of the analysis to two dimensions. Contrastingly, FracNet adopts a fully data-driven methodology. By moving away from the dependency on rib centerlines, FracNet overcomes the difficulties and inaccuracies involved in translating 3D structures into

TABLE IV

**SOLUTION SUMMARY IN THE RIB FRACTURE CLASSIFICATION TRACK.** EACH OF THE SOLUTIONS IS SUMMARIZED IN THE FOLLOWING ASPECTS: THE TYPE OF NEURAL NETWORK (2.5D / 3D), PRETRAINING, BACKBONE, INPUT RESOLUTION, DATA AUGMENTATION METHODS, TRAINING LOSS, AND SPECIAL REMARKS

Team	2.5D / 3D	Pretraining	Backbone	Input Resolution	Data Augmentation	Loss	Remarks
UCIrvine (CT1)	3D	No	NoduleNet [74]	64×64×64	Random flip, rotation, scaling and transition	Cross-entropy, Dice	Segmentation before classification
DCC (CT2)	3D	Med3D [71]	ResNet50 [44]	96×96×24	Random rotation and flip	Cross-entropy	Dilated convolutions [72], auto context [73]
DeepBlueAI (CT3)	3D	No	Custom CNN	64×64×64	None	Cross-entropy, Dice	Segmentation before classification, SE [75]
CCCS (CT4)	3D	No	ResNet18 [44]	128×128×64	None	Cross-entropy	Class-weighted loss

TABLE V

**A PERFORMANCE COMPARISON OF RIB FRACTURE CLASSIFICATION TASK ON THE RIBFRAC TEST SET.** WE REPORT THE PREDICTION-AWARE F1 SCORE, TARGET-AWARE F1 SCORE AND OVERALL F1 SCORE FOR EACH CATEGORY, AS WELL AS THEIR MACRO-AVERAGE. THE BEST METRICS ARE HIGHLIGHTED IN **BOLD**. THE METRIC FOR RANKING IS HIGHLIGHTED IN **BLUE**

Method	Prediction-Aware F1 Score				Target-Aware F1 Score				Overall F1 Score				Avg ↑		
	BK ↑	DP ↑	ND ↑	SG ↑	Avg ↑	BK ↑	DP ↑	ND ↑	SG ↑	Avg ↑	BK ↑	DP ↑	ND ↑	SG ↑	
UCIrvine	0.3514	0.5503	0.5324	0.0833	0.3793	0.2114	0.5041	0.4744	0.0714	0.3153	0.2063	0.4844	0.4554	0.0690	<b>0.3038</b>
DCC	0.3478	0.4869	0.5249	0.0784	0.3595	0.2697	0.4693	0.4969	0.0741	<b>0.3275</b>	0.1791	0.3790	0.3980	0.0678	0.2560
DeepBlueAI	0.2500	0.6839	0.6099	0.2500	<b>0.4485</b>	0.0597	0.5550	0.4433	0.0976	0.2889	0.0377	0.4309	0.3857	0.0784	0.2332
CCCS	0.0000	0.4356	0.7424	0.0690	0.3117	0.0000	0.3929	0.7143	0.0625	0.2924	0.0000	0.2619	0.5782	0.0625	0.2257

2D representations, a common challenge in rib unfolding. This strategy aligns more closely with the complex, three-dimensional nature of rib fractures. Consequently, FracNet leverages the full spatial context provided by 3D CT scans for more accurate and reliable detection of fractures. This is especially pivotal in identifying subtle or complex fractures that might be missed or wrongly interpreted in 2D analyses. This approach is not only foundational to FracNet but has also become the basis for almost all detection solutions in the RibFrac Challenge, focusing on direct end-to-end learning and prediction of 3D instance segmentation of rib fractures.

The operational phases of FracNet include pre-processing, sliding-window prediction, and post-processing.

- Pre-processing.** This phase enhances detection efficiency by extracting bone areas using morphological operations like thresholding and filtering, preserving the original spacing of thin-section CT scans. Input voxel intensities are adjusted to a specific bone window (level=450, width=1100) and normalized to a range of  $[-1, 1]$ .
- Sliding-window prediction.** FracNet employs a specialized 3D UNet for rib fracture segmentation in a sliding-window manner. To accommodate the size of whole-volume scans, which may exceed standard GPU memory capacities, the scans are divided into  $R \times R \times R$  patches with a  $0.75R$ -voxel stride, processed sequentially through the network. Here,  $R$  denotes the size of the sliding window. The cumulative segmentation outcome is derived by assembling these individual patch predictions, maintaining the maximum values in overlapping areas.
- Post-processing.** To reduce false positives, small predictions (under 200 voxels) are excluded. Additionally, spine regions identified in the raw segmentation are removed. Detection proposals are generated by binarizing the post-processed segmentation at a softmax confidence

threshold (0.1) and computing connected components on this binary segmentation. Each connected component is considered a detection proposal, with its probability calculated from the average segmentation scores within the component.

### B. Extending FracNet to FracNet+

**1) Integration With Point-Based Rib Segmentation:** Although rib unfolding may not be the ideal method, the ribs can still have an active role in fracture detection. Therefore, following the development of FracNet, we continue to evolve our methodologies by creating the RibSeg dataset and a point-based rib segmentation technique for rapid rib segmentation [39], [40]. The basic concept is as follows:

We address the sparsity of ribs in 3D volumes, which comprise less than 0.5% of the voxels, and the high Hounsfield Unit (HU) values characteristic of bones in CT scans. Our approach involves designing a point cloud-based model to segment ribs on binarized sparse voxels. Initially, we set a threshold of 200 HU to coarsely filter out non-bone voxels. These binarized volumes are then randomly downsampled and converted into point sets, simplifying computation before processing through the network. We utilize a point cloud neural net as the backbone and demonstrate robust performance in sparse 3D point cloud segmentation tasks. With RibSeg, we can swiftly segment ribs. For instance, by considering only a subset of points (30K), rib segmentation can be completed in under 1 second, in stark contrast to the over 70 seconds required by sliding-window based nnUNet [76], while maintaining higher accuracy [40].

A naive method to integrate RibSeg with FracNet is by replacing the bone extraction step in FracNet, which is based on morphological operations and can only roughly delineate bone areas, with a more precise rib extraction using RibSeg.

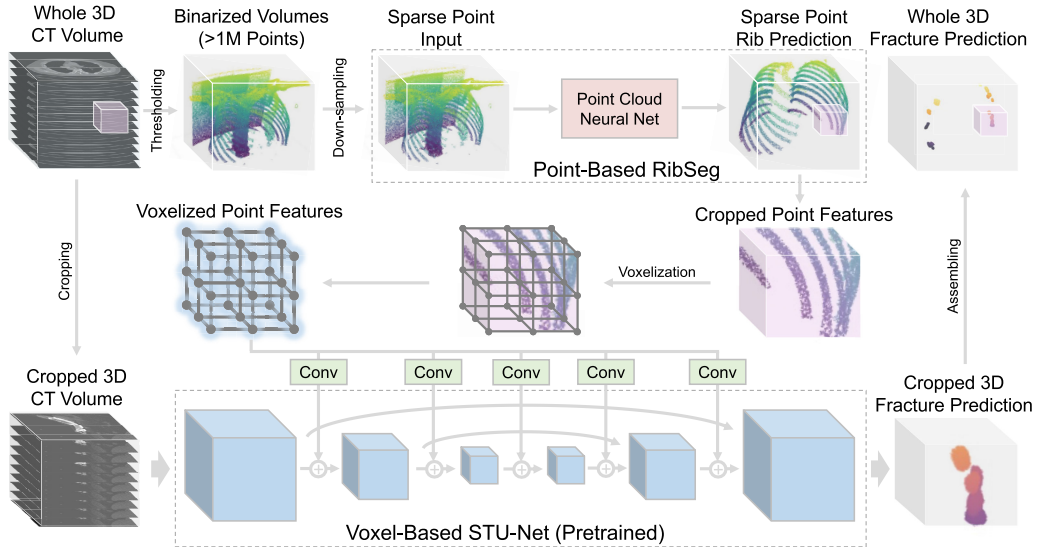


**Fig. 11.** A schematic overview of the FracNet+ framework, illustrating the dual-branch architecture for rib fracture segmentation. The top branch, the point-based rib segmentation network (RibSeg [39], [40]), processes binarized and downsampled point clouds from the whole 3D CT volume to predict ribs. The bottom branch, a voxel-based rib fracture segmentation network (a pretrained STUNet [41]), operates on cropped 3D CT volumes from rib areas to predict fractures. The voxelized point features from RibSeg are fused with the voxel-based fracture predictions to enhance the final fracture detection by integrating global context and local anatomical details.

This enables us to predict fractures using a sliding-window approach around the rib predictions, enhancing the accuracy and efficiency of the fracture detection process.

**2) Voxel-Point Fusion With Rib Segmentation:** Beyond the aforementioned naive integration, considering the guiding role of ribs in rib fracture segmentation, we propose a deep integration of features from the point-based rib segmentation network into the voxel-based fracture segmentation network. Specifically, our approach involves the following steps:

The FracNet+ network consists of two branches. The first branch is the point-based rib segmentation network, with an input-output mapping of  $N \times 3 \rightarrow N \times 1$ . This network processes a sparse point cloud sampled from the thresholded whole CT volume, outputting a score for each point indicating whether it is part of a rib. Here,  $N$  represents the number of input points. Based on the rib segmentation output, we sample a coordinate and expand a window of size  $R \times R \times R$  centered at it. Using this window, we crop the corresponding range of the original image to input into the second branch for fracture segmentation. Additionally, we crop the feature  $F_p \in \mathbb{R}^{M \times C_p}$  from the preceding layer of the output for subsequent feature integration, where  $M$  and  $C_p$  denote the number of the cropped point cloud and feature channel, respectively.

The second branch is a voxel-based segmentation network with a UNet-like structure that inputs the cropped CT volume and outputs fracture segmentation scores for each voxel, *i.e.*,  $1 \times R \times R \times R \rightarrow 1 \times R \times R \times R$ , where  $R$  represents the window size used to crop the CT volume. At multiple stages of the voxel network, we integrate the feature  $F_p$  from the point branch. Specifically, for one of the voxel feature stages  $F_v \in \mathbb{R}^{C_v \times r \times r \times r}$ , we first voxelize  $F_p$  into voxel features  $F'_p \in \mathbb{R}^{C_p \times r \times r \times r}$ . In this step, features falling into the same voxel in the  $r \times r \times r$  grid are pooled together to form a single feature, which is a differentiable operation [77].  $r$  refers to the feature voxel size in STU-Net. Afterwards, we use a  $1 \times 1 \times 1$

convolutional layer to transform  $F'_p$  into  $C_v$  channels, and then add it to  $F_v$ . Mathematically,

$$F'_p = \text{Voxelization}(F_p) \in \mathbb{R}^{C_p \times r \times r \times r},$$

$$F'_v = F_v + \text{Conv}(F'_p) \in \mathbb{R}^{C_v \times r \times r \times r}.$$

The resulting feature  $F'_v$  combines the voxel branch features with the voxelized point branch features. Notably, although both  $F_v$  and  $F_p$  are derived from the cropped patch,  $F_p$  inherently possesses a global context, as its input is global. This means that the high-level information in the point cloud network has already aggregated features extending beyond the range of the cropped patch. Consequently, these enhanced features, particularly those emphasizing the rib area, can significantly improve the network's ability to segment fractures along the ribs. These fusion layers are applied across multiple stages of the voxel segmentation network. The integration of global and local features from both point and voxel branches in FracNet+ aims to capitalize on the strengths of both modalities, thereby enhancing the overall performance and accuracy of rib fracture segmentation.

**3) Large-Scale Pre-Trained Model:** A recent trend in medical imaging has been the development of large-scale pre-trained models, also referred to as medical large vision models [78], [79]. These models are trained on extensive datasets, enabling them to learn strong representations of medical images, which can significantly enhance their performance on specific tasks without extensive task-specific training.

One of the key benefits of these large pre-trained models is their ability to act as a “free lunch” to boost the performance of applications in medical imaging. By leveraging the rich features learned from vast and varied data, they can provide a strong foundation for further fine-tuning on more specialized tasks, such as the segmentation of specific anatomical structures. In the context of our application, we have chosen STUNet [41], [80], a UNet-based model pre-trained on the

TotalSegmentator dataset [80], pre-trained for the segmentation of 104 different organs from CT scans, notably including the ribs. It is worth mentioning that the rib labels in the TotalSegmentator [80] were derived from models trained on our RibFrac dataset with RibSeg labels [39], [40]. The choice of STUNet as the pre-trained model is strategic, as the extensive pre-training on large-scale CT scans with a broad range of anatomical structures provides a sophisticated understanding of the surrounding anatomy. One of the key reasons for its selection is its powerful multi-organ pretraining model for CT imaging, based on TotalSegmentator [80], which includes rib segmentation. Additionally, its training pipeline is built upon the widely-used nnU-Net [76], offering better modularity and extensibility compared to the original, more tightly encapsulated TotalSegmentator codebase. These advantages made STUNet a more practical choice for our work. To adapt STUNet for rib fracture detection, we employed a full model fine-tuning approach, as the annotations of rib fractures on the RibFrac dataset is sufficiently large.

### C. Model Details

In this section, the method details will be outlined, encompassing the model architecture, training, and inference.

The FracNet+ architecture integrates two specialized branches: a point branch dedicated to rib segmentation and a voxel branch for rib fracture segmentation. The point branch is designed to work with any point cloud neural network as its backbone; in our implementation, we utilize PointNet++ [81] to process inputs of 30,000 points. For the voxel branch, we employ a pretrained STUNet Base [41] ( $R = 128$ ) to maintain a balance between accuracy and computational efficiency.

The two branches are jointly trained. It involves random point sampling for the point network and random cropping windows from rib for the voxel network. Both are trained using a combination of cross-entropy and Dice loss with rib and fracture segmentation as ground truth, respectively, without additional data augmentation beyond random sampling.

During inference, the FracNet+ first carries out the point branch computation to segment the ribs and caches the features from the last layer. Subsequent to this, center coordinates are sampled on the predicted rib segmentation to ensure that the sliding windows cover the entire rib area. The model then proceeds to the point-voxel fusion within these windows and predicts the rib fracture segmentation.

### D. Internal Experiments

In this section, we evaluated the performance of our internal methods, which include FracNet [38], FracNet+, and their variants for ablation study. This evaluation also encompassed models using only RibSeg, through either naive integration or point-voxel fusion, as well as models using only STUNet, whether with random initialization or pretrained on TotalSegmentator. It is crucial to highlight that all our internal methods are one-stage approaches that leverage a neural network for segmentation and determine the detection proposal confidence by calculating the average confidence across the segmented regions. Besides, the RibFrac Challenge test set includes

40 additional cases beyond the dataset utilized in [38]. This discrepancy accounts for the different metrics reported when compared to the original publication [38].

Considering the computational demands of RibFrac's large-scale dataset, we selected a few representative baseline methods [76], [82], [83] for comparison in the paper, with a particular emphasis on the widely-used nnU-Net [76]. As analyzed in [84], nnU-Net outperforms many newer methods in terms of both performance and stability, and we believe it serves as a sufficiently robust baseline. The results in Tab. VI indicate that while FracNet significantly outperforms 3D FCN [82] and 3D DeepLab [83], FracNet+, an expansion of FracNet, demonstrates even greater effectiveness. The results of nnU-Net [76] are very close to those of FracNet w/ STUNet (Random), as the training pipeline of STUNet also follows the nnU-Net [76] framework. This is evident whether through the integration of RibSeg or the use of the large-scale pretrained STUNet, both of which notably surpass the original FracNet. Naive integration of rib outputs in pre- and post-processing, as seen in FracNet w/ RibSeg (Naive) vs. FracNet, also improves model performance, especially in reducing false positives, though it does not improve sensitivity. However, employing a point-voxel feature fusion to enhance rib features—FracNet w/ RibSeg (Fusion) vs. FracNet w/ RibSeg (Naive)—further boosts network performance, with a significant increase in sensitivity at low false positive levels and an overall rise in the highest sensitivity achieved. On the other hand, substituting the voxel network with STUNet, even without using pretrained weights, shows a slight performance increase, as seen in FracNet w/ STUNet (Random) vs. FracNet. Introducing pretrained weights—FracNet w/ STUNet (Pretrained) vs. FracNet w/ STUNet (Random)—further improves overall performance. However, it is observed that merely changing the network structure or incorporating pretraining does not have as marked an effect as integrating RibSeg, as shown in FracNet w/ STUNet (Pretrained) vs. FracNet w/ RibSeg (Fusion), which highlights the usefulness of domain knowledge. Their effects seem to be complementary: while the former may further increase sensitivity, it does not significantly reduce false positives. Finally, FracNet+, which is essentially FracNet w/ RibSeg (Fusion) w/ STUNet (Pretrained), combines the advantages of both modifications and achieves the best.

In terms of computational cost, FracNet+ is comparable to FracNet [38]. Among its components, the voxel branch incurs the highest computational cost due to the sliding windows. However, the added point branch is highly efficient because RibSeg [40] operates on the global sparse volume without sliding windows. As a result, the additional processing time introduced by the point branch is less than 1s. On the same machine used for previous FracNet time testing—a single NVIDIA GTX 1080Ti with an Intel Xeon E5-2650 and 128 GB of memory—FracNet+ achieves an average inference time of 33.6s, compared to FracNet's average of 31.2s.

It is noteworthy that FracNet+ achieves higher sensitivity and finer segmentation compared to two human radiologists (R1, R2). Even though FracNet+ may yield more false

TABLE VI

**INTERNAL RIB FRACTURE DETECTION METHODS ON THE RIBFRAC TEST SET.** WE REPORT THE FROC METRICS (%), MAX SENSITIVITY (%) AND AVG FALSE POSITIVES FOR RIB FRACTURE DETECTION, IOU (%) AND DICE (%) FOR RIB FRACTURE SEGMENTATION. THE BEST METRICS ARE HIGHLIGHTED IN **BOLD**

Method	Detection FROC (Sensitivities @FP levels)						Detection Auxillary Metrics		Segmentation	
	0.5 ↑	1 ↑	2 ↑	4 ↑	8 ↑	Avg ↑	Max Sensitivity ↑	Avg FP ↓	IoU ↑	Dice ↑
<i>Internal Baselines</i>										
3D FCN [82]	59.58	69.10	76.03	82.71	85.18	74.52	85.18	7.96	40.37	58.49
3D DeepLab [83]	63.38	71.90	79.13	86.51	88.68	77.92	88.68	7.05	41.57	60.99
FracNet [38]	65.68	74.40	81.63	88.81	90.28	80.16	90.28	6.21	46.87	63.79
nnU-Net [76]	65.95	74.71	82.03	89.12	90.62	80.49	90.58	6.04	46.99	63.93
<i>Extending FracNet to FracNet+</i>										
FracNet w/ RibSeg (Naive) [39], [40]	69.90	75.96	82.52	89.50	90.58	81.69	89.65	4.91	48.69	65.77
FracNet w/ RibSeg (Fusion) [39], [40]	73.56	78.22	83.86	89.92	90.77	83.27	91.29	4.34	49.59	66.81
FracNet w/ STUNet (Random) [41]	66.20	75.04	82.40	89.46	90.94	80.81	90.83	5.89	47.15	64.10
FracNet w/ STUNet (Pretrained) [41]	67.42	76.05	83.17	90.14	91.17	81.59	91.76	5.32	47.72	64.72
<b>FracNet+</b>	<b>75.67</b>	<b>79.22</b>	<b>84.32</b>	<b>90.82</b>	<b>91.43</b>	<b>84.29</b>	<b>92.17</b>	<b>4.22</b>	<b>50.02</b>	<b>67.22</b>
<i>Comparing with Human Experts</i>										
R1	-	-	-	-	-	-	79.12	1.22	46.62	63.55
R2	-	-	-	-	-	-	75.87	0.86	35.93	52.32

positives than human experts, human radiologists can easily pinpoint lesions with fewer false positives, thereby enhancing the sensitivity of their diagnoses [38].

Additionally, though DT1 and DT2 surpass the performance of our earlier internal version FracNet, with the incorporation of recent advancements, FracNet+ demonstrates superior effectiveness. Even when compared to post-challenge results (A1 and A2), FracNet+, as a one-stage method, holds its ground in many metrics, particularly in segmentation accuracy and false positive rates. Considering the potential use of challenge tricks, such as multi-stage models (including false positive reduction) and ensemble techniques, there is room for further improvement in FracNet+. However, a direct comparison may not be entirely fair due to our later development timeline and complete access to the data as the authors. Therefore, we have refrained from employing too many challenge tricks and have chosen to present our internal results and challenge results in separate tables to maintain clarity and fairness.

Nevertheless, our analysis indicates that while simply replacing the network may yield improvements, it does not achieve the integration with rib segmentation. This finding underscores the beneficial role of rib segmentation in enhancing fracture detection.

## VII. LIMITATIONS AND FUTURE WORK

The single-center nature of our dataset is a clear limitation. Additionally, due to the requirement for public accessibility, we ensured complete anonymization during data transfer from the hospital’s information system. Equipment details were not part of the required information by design and, therefore, were not retained. This limitation also makes it difficult to analyze differences between vendors. Nonetheless, as the first open-access dataset in this field, we believe that the scale, quality, and impact of RibFrac remain significant.

The classification task not yet reaching clinical applicability is also a limitation. One reason for this challenge is the inherent difficulty of the classification task itself, as highlighted in Sec. V-C. Another contributing factor is that the evaluation

of the classification task is tightly coupled with the detection task, which further increases its complexity. To enable more focused analysis of the fracture classification task, we have simplified and extracted it as an independent dataset, FractureMNIST3D, in a separate work, MedMNIST [85]. In our internal benchmarking on this dataset, although the settings are not entirely identical, the classification task achieved an AUC of approximately 0.75. As noted, this task remains challenging. By providing open datasets, conducting internal benchmarking, and performing meta-analyses on challenge results, we aim to leverage the collective efforts of the research community to address this problem more effectively.

The challenge operates as a result submission one (requiring only prediction results) rather than a model submission one, which is also a limitation. Under this design, we are unable to gain additional post-challenge insights, such as model runtime or computational costs. Moreover, certain robustness analyses are difficult to conduct, despite recent meta-analyses highlighting their sensitivity [86], [87], [88].

To address these limitations, we are actively working on RibFrac v2, which will feature larger-scale and more diverse data, better-designed evaluations, and improved baseline models. This effort aims to resolve many of the current shortcomings identified by both ourselves and the reviewers.

Network backbones can still be explored for the RibFrac benchmark. Following the official challenge, several new architectures have emerged, such as vision transformers (ViT) [89]. To our knowledge, no published works have attempted to use ViT as a backbone for RibFrac. This may be due to ViT’s inconsistent performance across medical imaging tasks, as noted in [84]. Nonetheless, ViT or other new architectures, particularly when pre-trained, represent promising avenues for improvement and warrant further exploration in future studies.

## VIII. CONCLUSION

In conclusion, the RibFrac Challenge has served as a valuable benchmark and research resource for AI-assisted rib fracture detection and diagnosis. With its extensive dataset and evaluation platform, the challenge has addressed previous

limitations and facilitated significant progress in rib fracture detection. Promising results have been achieved, showing that AI can enhance accuracy and reduce interpretation time. However, there is still room for improvement in rib fracture classification solutions. The challenge has paved the way for future research and integration of AI tools into radiology workflows. Overall, the RibFrac Challenge has played a crucial role in advancing the field and will continue to drive improvements in rib fracture analysis.

As an independent technical contribution, we develop a strong internal method FracNet+. We integrate several post-challenge advancements, including the development of a point-based rib segmentation technique and the emergence of large-scale pre-trained networks for 3D medical imaging, yielding competitive results in rib fracture detection and highlighting the importance of rib segmentation in this field.

Future research directions should concentrate on several areas. A primary goal is to develop unified approaches that seamlessly integrate rib labeling, anatomical centerline extraction, and fracture diagnosis. Moreover, enhancing the classification performance of different types of rib fractures is crucial. Despite advancements in fracture detection, accurately classifying various fracture types remains a complex challenge. Insights gained from this study of technical hurdles and existing methodologies will be invaluable for future endeavors in this aspect of rib fracture classification. Additionally, the development and validation of these models on multi-center data are of high importance. Addressing these future directions will not only expedite faster and more precise diagnoses but also enhance patient outcomes by enabling clinicians to make well-informed treatment decisions based on the severity and specific type of rib fractures. Continued collaboration, dataset expansion, and advancements in deep learning techniques will play vital roles in driving progress in rib fracture analysis and bringing us closer to clinically applicable solutions.

## APPENDIX

### *A. Summary of Rib Fracture Detection Solutions*

**1) Team lungseg2020 (DT1):** Mask-RCNN [66] with FPN [90] and ResNet-50 [44] backbone is extended from 2D to 2.5D for rib fracture detection and segmentation. Since it is a 2.5D method, the 3D CT scans are split into slices, resulting in 44,000 positive samples and 11,000 negative samples in the training set. Positive and negative samples are randomly selected with a 1:1 ratio during training. Horizontal flip is employed for training time augmentation, and the model is pretrained on ImageNet. Considering the relevance of adjacent slices in 3D CT scans, multiple adjacent slices are used as input to capture more contextual information, while the network outputs the prediction result of the middle slice. Experiments on the relationship between model performance and the number of adjacent slices input are conducted, and it is found that 15 is the optimal choice. During inference, each slice in a CT scan is processed independently. Predictions below a certain threshold are disregarded. 2D predictions are merged into 3D based on connectivity, and the 3D prediction score is calculated as the average of the 2D prediction scores.

**2) Team DCC (DT2):** A cascaded rib fracture detection pipeline is proposed, consisting of a 2D slice-level detection network and a 3D patch-level segmentation network. The 2D detection network uses the Mask-RCNN [66] model with ResNet [44] and HRNet [67] pretrained on ImageNet as the backbone. FPN [90] structure is added to enable multi-scale prediction. Random horizontal flip augmentation is applied to make the model learn invariant features. For the 3D segmentation network, UNet [69] is employed to capture stereoscopic features using an iterative training strategy. The predicted masks of Mask-RCNN are combined with the ground truth to obtain the training samples for UNet. The CT scans are cropped according to the center of each connected component before being fed into the network. Random rotation and flipping operations are performed for data augmentation. For model finetuning, predicted masks are integrated with ground truths to obtain new training samples.

**3) Team FakeDoctor (DT3):** A two-stage rib fracture detection pipeline is proposed. It uses a ResUNet [68] structure for rib fracture segmentation, followed by a classification model to predict the segmentation results. The down-sampling stage of the nnUNet [76] model framework is replaced with ResUNet. Attention module and inflated module are applied to enlarge the subsampling receptive field. Combined binary cross-entropy loss and Dice loss are used as the loss function. In the post-processing stage of the segmentation model, prediction masks with smaller areas than the threshold are eliminated, while the remaining prediction masks are expanded to be slightly larger than the fracture area. In the classification model stage, the predicted masks are cropped and normalized through an adaptive pooling layer before being fed into a VGG [91] network. The confidence level of each prediction mask is obtained after classification. Conventional data augmentation methods such as random rotation, translation, cutting, and blurring are employed.

**4) Team UCIrvine (DT4):** A segmentation-based model with model ensembling techniques is used for rib fracture detection. Two 3D UNet [69] models are ensembled, one using binary cross-entropy loss and the other using Dice loss. The probability map is filtered with a threshold of 0.35, and each connected component is considered as an instance.

**5) Team MIDILab (DT5):** An ensemble of 3D UNets [69] followed by morphological operations is applied for rib fracture detection. The model is based on a residual 3D UNet [92], where all skip connections use element-wise addition instead of concatenation, and each module contains its own skip connection. The segmentation result is the voxel-wise mean of two residual 3D UNets, one trained on binary cross-entropy loss and the other on Dice loss [93], [94]. For post-processing, each prediction is upsampled to the dimension of the original CT scans. The prediction is binarized with a threshold, and missing voxels in connected fracture regions are filled in with a morphological binary closing operation. Small predicted fracture instances smaller than  $512 \text{ mm}^3$  are removed to avoid over-prediction. In the final binary prediction, instance labels are assigned by identifying and numbering the connected components. The post-processing hyperparameters that maximize

the validation FROC are determined by a grid search and used in all future runs.

**6) Team CCCCCS (DT6):** A 2D residual UNet [69] is employed to segment rib fractures on 2D slices, followed by splicing the predictions into 3D as the post-processing operation. For data pre-processing, the ribs and their surrounding areas are extracted as input to address the problem of class label imbalance. The coronal slices are binarized with a threshold of 110 HU. A morphological dilation operation is applied to preserve soft tissues around the ribs. The binary images serve as the region-of-interest (ROI) masks, which are multiplied with the slices to obtain training data. Two slices of each annotation at the head and tail in the axial plane are disregarded to ensure that the rib fractures are clearly visible. The network architecture is a residual 2D UNet, with hybrid dilated convolution [72] used to increase the receptive field. A two-stage training strategy is adopted to detect small rib fracture targets and reduce false-positive predictions simultaneously. Modified generalized Dice loss (GDL) [94] is used to train a model with high recall, and then Tversky loss [95] is employed for false-positive reduction. In the post-processing stage, a morphological dilation operation on spliced 2D slices in the axial plane is performed to eliminate crevices in predictions across slices.

### B. Summary of Rib Fracture Classification Solutions

**1) Team UCIrvine (CT1):** 3D UNet [69] with binary cross entropy is utilized for rib fracture segmentation. To limit the number of false positives, the probability map is filtered with a threshold of 0.95. For classification, the backbone of NoduleNet [74] is followed by three fully connected layers. A dropout layer is added between the last two fully connected layers to suppress overfitting. For data pre-processing, logarithm transformation is applied to the filtered and normalized CT scans, to balance out the effect of long tail data distribution. Each rib fracture in training and validation data is cropped into a 3D bounding cuboid with 4 extra pixels in each direction, with cuboid labeled -1 dropped. Random flipping, rotation, scaling and translation operations are conducted for training time data augmentation.

**2) Team DCC (CT2):** 3D ResNet-50 [44] pretrained on Med3D [71] is used for rib fracture classification. Dilated convolutions [72] are applied in residual blocks to increase the receptive field while keeping the feature resolution. An auto-context mechanism [73] is adopted, where CT scans are integrated with masks generated by the segmentation model as the input of 3D ResNet-50 model. It demonstrated that the guidance of rib fracture mask could boost the classification performance. Random rotation and flipping operations are conducted to alleviate the over-fitting problem.

**3) Team DeepBlueAI (CT3):** DeepMedic [96], a dual pathway structure, is employed as the baseline of rib fracture detection. A 3D CNN with parallel convolution pathways extracts highly accurate and soft segmentation features, followed with a fully connected 3D conditional random fields (CRF) to generate segmentation labels. The dual pathways share the same structure but have different input resolutions, so that both local and contextual information are incorporated. Shortcuts connections are utilized in the structure, similar

as those in ResNet [44], to improve the training efficiency and boost performance. The segmentation features of the dual pathway 3D CNN are fed into fully connected layers, and then a 3D fully connected CRF with spatial regularization is used to generate smooth segmentation labels. Small connected components are removed for false-positive reduction.

**4) Team CCCCCS (CT4):** 3D ResNet-18 [44] with weighted cross-entropy loss is applied for rib fracture classification. The classification method is based on the segmented regions in rib fracture detection task, which is described in the detection track. The 3D variant version of ResNet-18 is used as the backbone. Due to the extreme imbalance between classes, weighted cross-entropy loss is adopted, with the normalized reciprocal of the number of samples in each category in the training set as the weight.

### ACKNOWLEDGMENT

Jiancheng Yang, Rui Shi, Xiaoyang Huang, and Bingbing Ni are with the Department of Electronic Engineering, Shanghai Jiao Tong University, Shanghai 200240, China (e-mail: yang.jiancheng@outlook.com; shi-rui@sjtu.edu.cn; huangxiaoyang@sjtu.edu.cn; nbbingbing@sjtu.edu.cn).

Liang Jin is with the Radiology Department, Huadong Hospital affiliated to Fudan University, Shanghai 200031, China, also with the Huashan Hospital affiliated to Fudan University, Shanghai 200031, China, and also with Shanghai Key Laboratory of Forensic Medicine and the Key Laboratory of Forensic Science, Academy of Forensic Science, Ministry of Justice, Shanghai 200063, China (e-mail: jin\_liang@fudan.edu.cn).

Kaiming Kuang is with Diane Technology, Shanghai 200051, China, and also with the Department of Computer Science and Engineering, University of California, San Diego, CA 92093 USA (e-mail: kakuang@ucsd.edu).

Donglai Wei is with Boston College, Chestnut Hill, MA 02467 USA (e-mail: donglai.wei@bc.edu).

Shixuan Gu and Hanspeter Pfister are with the Department of Computer Science, Harvard University, Cambridge, MA 02138 USA (e-mail: shixuangu@g.harvard.edu; pfister@seas.harvard.edu).

Jianying Liu and Pengfei Liu are with Huiying Medical Technology (Beijing) Company Ltd., Beijing 100029, China (e-mail: liujianying@huiyihuiying.com; liupengfei@huiyihuiying.com).

Zhizhong Chai and Yongjie Xiao are with ImsightMed, Shenzhen 518000, China (e-mail: chaizhizhong@imsightmed.com; xiaoyongjie@imsightmed.com).

Hao Chen is with the Department of Computer Science and Engineering, The Hong Kong University of Science and Technology, Hong Kong, SAR, China (e-mail: jhc@cse.ust.hk).

Liming Xu and Bang Du are with the College of Computer Science and Technology, Zhejiang University, Hangzhou 310027, China (e-mail: Sunrise2019@zju.edu.cn; dubangcompany@gmail.com).

Xiangyi Yan and Hao Tang are with the Department of Computer Science, University of California, Irvine, CA 92697 USA (e-mail: xiangyy4@uci.edu; htang6@uci.edu).

Adam Alessio is with the Department of Biomedical Engineering, Michigan State University, East Lansing, MI 48824 USA (e-mail: aalessio@msu.edu).

Gregory Holste is with the Department of Electrical and Computer Engineering, The University of Texas at Austin, Austin, TX 78712 USA, and also with the Department of Biomedical Engineering, Michigan State University, East Lansing, MI 48824 USA (e-mail: gholste@utexas.edu).

Jiapeng Zhang and Xiaoming Wang are with the Department of Control Science and Engineering, University of Shanghai for Science and Technology, Shanghai 200093, China (e-mail: mnrsmjz@126.com; wangxm7909@126.com).

Jianye He and Lixuan Che are with DeepBlue Technology (Shanghai) Company Ltd., Shanghai 200336, China (e-mail: hejycomeon@163.com; 837116734@qq.com).

Ming Li is with the Radiology Department, Huadong Hospital affiliated to Fudan University, Shanghai 200031, China, and also with the Institute of Functional and Molecular Medical Imaging, Shanghai 200040, China (e-mail: minli77@163.com).

## REFERENCES

- [1] K. J. Brasel, C. E. Guse, P. Layde, and J. A. Weigelt, "Rib fractures: Relationship with pneumonia and mortality\*," *Crit. Care Med.*, vol. 34, no. 6, pp. 1642–1646, Jun. 2006.
- [2] C. E. Witt and E. M. Bulger, "Comprehensive approach to the management of the patient with multiple rib fractures: A review and introduction of a bundled rib fracture management protocol," *Trauma Surg. Acute Care Open*, vol. 2, no. 1, Jan. 2017, Art. no. e000064.
- [3] I. Baiu and D. Spain, "Rib fractures," *Jama*, vol. 321, no. 18, p. 1836, 2019.
- [4] J. Peek et al., "Epidemiology and outcome of rib fractures: A nationwide study in The Netherlands," *Eur. J. Trauma Emergency Surg.*, vol. 48, no. 1, pp. 265–271, Feb. 2022.
- [5] K. Kuo and A. M. Kim, "Rib fracture," in *StatPearls [Internet]*. St. Petersburg, FL, USA: StatPearls Publishing, 2021.
- [6] H. M. Ingoe, W. Eardley, C. McDaid, A. Rangan, T. Lawrence, and C. Hewitt, "Epidemiology of adult rib fracture and factors associated with surgical fixation: Analysis of a chest wall injury dataset from England and Wales," *Injury*, vol. 51, no. 2, pp. 218–223, Feb. 2020.
- [7] B. S. Talbot, C. P. Gange, A. Chaturvedi, N. Klionsky, S. K. Hobbs, and A. Chaturvedi, "Traumatic rib injury: Patterns, imaging pitfalls, complications, and treatment," *RadioGraphics*, vol. 37, no. 2, pp. 628–651, Mar. 2017.
- [8] J. Peek et al., "Traumatic rib fractures: A marker of severe injury. A nationwide study using the national trauma data bank," *Trauma Surgery Acute Care Open*, vol. 5, no. 1, Jun. 2020, Art. no. e000441.
- [9] M. Kolopp et al., "Automatic rib unfolding in postmortem computed tomography: Diagnostic evaluation of the OpenRib software compared with the autopsy in the detection of rib fractures," *Int. J. Legal Med.*, vol. 134, no. 1, pp. 339–346, Jan. 2020.
- [10] L. Jin et al., "Low-dose CT examination for rib fracture evaluation: A pilot study," *Medicine*, vol. 97, no. 30, 2018, Art. no. e11624.
- [11] N. Banaste, B. Caurier, F. Bratan, J.-F. Bergerot, V. Thomson, and I. Millet, "Whole-body CT in patients with multiple traumas: Factors leading to missed injury," *Radiology*, vol. 289, no. 2, pp. 374–383, Nov. 2018.
- [12] H. Ringl et al., "The ribs unfolded—A CT visualization algorithm for fast detection of rib fractures: Effect on sensitivity and specificity in trauma patients," *Eur. Radiol.*, vol. 25, no. 7, pp. 1865–1874, Jul. 2015.
- [13] A. Blum, R. Gillet, A. Urbaneja, and P. Gondim Teixeira, "Automatic detection of rib fractures: Are we there yet?" *EBioMedicine*, vol. 63, Jan. 2021, Art. no. 103158.
- [14] A. Pinto et al., "Errors in imaging patients in the emergency setting," *Brit. J. Radiol.*, vol. 89, no. 1061, May 2016, Art. no. 20150914.
- [15] P. Dankerl, H. Seuss, S. Ellmann, A. Cavallaro, M. Uder, and M. Hammon, "Evaluation of rib fractures on a single-in-plane image reformation of the rib cage in CT examinations," *Academic Radiol.*, vol. 24, no. 2, pp. 153–159, Feb. 2017.
- [16] S. H. Cho, Y. M. Sung, and M. S. Kim, "Missed rib fractures on evaluation of initial chest CT for trauma patients: Pattern analysis and diagnostic value of coronal multiplanar reconstruction images with multidetector row CT," *Brit. J. Radiol.*, vol. 85, no. 1018, pp. e845–e850, Oct. 2012.
- [17] A. A. A. Setio et al., "Validation, comparison, and combination of algorithms for automatic detection of pulmonary nodules in computed tomography images: The LUNA16 challenge," *Med. Image Anal.*, vol. 42, pp. 1–13, Dec. 2017.
- [18] S. M. McKinney et al., "International evaluation of an AI system for breast cancer screening," *Nature*, vol. 577, no. 7788, pp. 89–94, Jan. 2020.
- [19] J. Yang et al., "Alignshift: Bridging the gap of imaging thickness in 3D anisotropic volumes," in *Proc. Int. Conf. Med. Image Comput. Comput.-Assist. Intervent.* Cham, Switzerland: Springer, 2020, pp. 562–572.
- [20] J. Yang, Y. He, K. Kuang, Z. Lin, H. Pfister, and B. Ni, "Asymmetric 3D context fusion for universal lesion detection," in *Proc. Int. Conf. Med. Image Comput. Comput.-Assist. Intervent.* Cham, Switzerland: Springer, 2021, pp. 571–580.
- [21] R. Xu, Y. Luo, B. Du, K. Kuang, and J. Yang, "Lssanet: A long short slice-aware network for pulmonary nodule detection," in *Proc. Int. Conf. Med. Image Comput. Comput.-Assist. Intervent.* Cham, Switzerland: Springer, 2022, pp. 664–674.
- [22] P. A. Keane and E. J. Topol, "With an eye to AI and autonomous diagnosis," *npj Digit. Med.*, vol. 1, no. 1, p. 40, Aug. 2018.
- [23] W. Zhao et al., "3D deep learning from CT scans predicts tumor invasiveness of subcentimeter pulmonary adenocarcinomas," *Cancer Res.*, vol. 78, no. 24, pp. 6881–6889, Dec. 2018.
- [24] J. Yang, R. Fang, B. Ni, Y. Li, Y. Xu, and L. Li, "Probabilistic radiomics: Ambiguous diagnosis with controllable shape analysis," in *Proc. Int. Conf. Med. Image Comput. Comput.-Assist. Intervent.* Cham, Switzerland: Springer, 2019, pp. 658–666.
- [25] K. Zhang, "Clinically applicable AI system for accurate diagnosis, quantitative measurements, and prognosis of COVID-19 pneumonia using computed tomography," *Cell*, vol. 181, no. 6, pp. 1423–1433, 2020.
- [26] J. Yang et al., "Hierarchical classification of pulmonary lesions: A large-scale radio-pathomics study," in *Proc. 23rd Int. Conf. Med. Image Comput. Comput.-Assist. Intervent.* Cham, Switzerland: Springer, 2020, pp. 497–507.
- [27] Y. Ding et al., "Improving the efficiency of identifying malignant pulmonary nodules before surgery via a combination of artificial intelligence CT image recognition and serum autoantibodies," *Eur. Radiol.*, vol. 33, no. 5, pp. 3092–3102, Dec. 2022.
- [28] W. L. Bi et al., "Artificial intelligence in cancer imaging: Clinical challenges and applications," *CA, Cancer J. Clinicians*, vol. 69, no. 2, pp. 127–157, 2019.
- [29] J. Yang, J. Chen, K. Kuang, T. Lin, J. He, and B. Ni, "MIA-Prognosis: A deep learning framework to predict therapy response," in *Proc. 23rd Int. Conf. Med. Image Comput. Comput.-Assist. Intervent.* Cham, Switzerland: Springer, 2020, pp. 211–220.
- [30] Y. Yang et al., "A multi-omics-based serial deep learning approach to predict clinical outcomes of single-agent anti-PD-1/PD-L1 immunotherapy in advanced stage non-small-cell lung cancer," *Amer. J. Transl. Res.*, vol. 13, no. 2, pp. 743–756, Feb. 2021.
- [31] M. Thies and M. L. Oelze, "Combined therapy planning, real-time monitoring, and low intensity focused ultrasound treatment using a diagnostic imaging array," *IEEE Trans. Med. Imag.*, vol. 41, no. 6, pp. 1410–1419, Jun. 2022.
- [32] J. Deng et al., "Genopathomic profiling identifies signatures for immunotherapy response of lung adenocarcinoma via confounder-aware representation learning," *iScience*, vol. 25, no. 11, Nov. 2022, Art. no. 105382.
- [33] E. J. Topol, "High-performance medicine: The convergence of human and artificial intelligence," *Nature Med.*, vol. 25, no. 1, pp. 44–56, Jan. 2019.
- [34] A. Urbaneja et al., "Automatic rib cage unfolding with CT cylindrical projection reformat in polytraumatized patients for rib fracture detection and characterization: Feasibility and clinical application," *Eur. J. Radiol.*, vol. 110, pp. 121–127, Jan. 2019.
- [35] A. Blum et al., "3D reconstructions, 4D imaging and postprocessing with CT in musculoskeletal disorders: Past, present and future," *Diagnostic Interventional Imag.*, vol. 101, no. 11, pp. 693–705, Nov. 2020.
- [36] T. Weikert et al., "Assessment of a deep learning algorithm for the detection of rib fractures on whole-body trauma computed tomography," *Korean J. Radiol.*, vol. 21, no. 7, p. 891, 2020.
- [37] Q.-Q. Zhou et al., "Automatic detection and classification of rib fractures on thoracic CT using convolutional neural network: Accuracy and feasibility," *Korean J. Radiol.*, vol. 21, no. 7, p. 869, 2020.
- [38] L. Jin et al., "Deep-learning-assisted detection and segmentation of rib fractures from CT scans: Development and validation of FracNet," *eBioMedicine*, vol. 62, Dec. 2020, Art. no. 103106.
- [39] J. Yang, S. Gu, D. Wei, H. Pfister, and B. Ni, "Ribseg dataset and strong point cloud baselines for rib segmentation from ct scans," in *Proc. 24th Int. Conf. Med. Image Comput. Comput.-Assist. Intervent.* Cham, Switzerland: Springer, 2021, pp. 611–621.
- [40] L. Jin et al., "RibSeg v2: A large-scale benchmark for rib labeling and anatomical centerline extraction," 2022, *arXiv:2210.09309*.
- [41] Z. Huang et al., "STU-net: Scalable and transferable medical image segmentation models empowered by large-scale supervised pre-training," 2023, *arXiv:2304.06716*.
- [42] Z. Zhou, Z. Fu, J. Jia, and J. Lv, "Rib fracture detection with dual-attention enhanced U-Net," *Comput. Math. Methods Med.*, vol. 2022, pp. 1–13, Aug. 2022.
- [43] G. Huang, Z. Liu, L. Van Der Maaten, and K. Q. Weinberger, "Densely connected convolutional networks," in *Proc. IEEE Conf. Comput. Vis. Pattern Recognit. (CVPR)*, Jul. 2017, pp. 2261–2269.
- [44] K. He, X. Zhang, S. Ren, and J. Sun, "Deep residual learning for image recognition," in *Proc. IEEE Conf. Comput. Vis. Pattern Recognit. (CVPR)*, Jun. 2016, pp. 770–778.
- [45] L. Yao et al., "Rib fracture detection system based on deep learning," *Sci. Rep.*, vol. 11, no. 1, p. 23513, Dec. 2021.
- [46] K. Duan, S. Bai, L. Xie, H. Qi, Q. Huang, and Q. Tian, "CenterNet: Keypoint triplets for object detection," in *Proc. IEEE/CVF Int. Conf. Comput. Vis. (ICCV)*, Oct. 2019, pp. 6568–6577.

- [47] F. Yu, D. Wang, E. Shelhamer, and T. Darrell, "Deep layer aggregation," in *Proc. IEEE/CVF Conf. Comput. Vis. Pattern Recognit.*, Jun. 2018, pp. 2403–2412.
- [48] C. Yang et al., "Development and assessment of deep learning system for the location and classification of rib fractures via computed tomography," *Eur. J. Radiol.*, vol. 154, Sep. 2022, Art. no. 110434.
- [49] B. Zhang et al., "Improving rib fracture detection accuracy and reading efficiency with deep learning-based detection software: A clinical evaluation," *Brit. J. Radiol.*, vol. 94, no. 1118, Feb. 2021, Art. no. 20200870.
- [50] X. Liu et al., "Clinical evaluation of AI software for rib fracture detection and its impact on junior radiologist performance," *Acta Radiologica*, vol. 63, no. 11, pp. 1535–1545, Nov. 2022.
- [51] X. H. Meng et al., "A fully automated rib fracture detection system on chest CT images and its impact on radiologist performance," *Skeletal Radiol.*, vol. 50, no. 9, pp. 1821–1828, Sep. 2021.
- [52] M. Kaiume et al., "Rib fracture detection in computed tomography images using deep convolutional neural networks," *Medicine*, vol. 100, no. 20, May 2021, Art. no. e26024.
- [53] A. Niiya et al., "Development of an artificial intelligence-assisted computed tomography diagnosis technology for rib fracture and evaluation of its clinical usefulness," *Sci. Rep.*, vol. 12, no. 1, p. 8363, May 2022.
- [54] A. Mansoor et al., "A generic approach to pathological lung segmentation," *IEEE Trans. Med. Imag.*, vol. 33, no. 12, pp. 2293–2310, Dec. 2014.
- [55] A. Fokin, J. Wycech, M. Crawford, and I. Puente, "Quantification of rib fractures by different scoring systems," *J. Surgical Res.*, vol. 229, pp. 1–8, Sep. 2018.
- [56] H. Wang, J. Bai, and Y. Zhang, "A relative thoracic cage coordinate system for localizing the thoracic organs in chest CT volume data," in *Proc. IEEE Eng. Med. Biol. Annu. Conf.*, Jan. 2005, pp. 3257–3260.
- [57] H. Shen and M. Shao, "A thoracic cage coordinate system for recording pathologies in lung CT volume data," in *Proc. IEEE Nucl. Sci. Symp. Conf. Rec.*, vol. 5, Oct. 2003, pp. 3029–3031.
- [58] G. Bier et al., "Enhanced reading time efficiency by use of automatically unfolded CT rib reformations in acute trauma," *Eur. J. Radiol.*, vol. 84, no. 11, pp. 2173–2180, Nov. 2015.
- [59] L. I. Abe et al., "High-speed point cloud matching algorithm for medical volume images using 3D Voronoi diagram," in *Proc. 7th Int. Conf. Biomed. Eng. Informat.*, Oct. 2014, pp. 205–210.
- [60] W. Wang et al., "MDU-net: A convolutional network for clavicle and rib segmentation from a chest radiograph," *J. Healthcare Eng.*, vol. 2020, pp. 1–9, Jul. 2020.
- [61] H. Guo, J. Zhang, K. Yan, L. Lu, and M. Xu, "Med-query: Steerable parsing of 9-DoF medical anatomies with query embedding," 2022, *arXiv:2212.02014*.
- [62] E. Schnider et al., "Improved distinct bone segmentation in upper-body CT through multi-resolution networks," 2023, *arXiv:2301.13674*.
- [63] D. Wu et al., "A learning based deformable template matching method for automatic rib centerline extraction and labeling in CT images," in *Proc. IEEE Conf. Comput. Vis. Pattern Recognit.*, Jun. 2012, pp. 980–987.
- [64] M. Lenga, T. Klinder, C. Bürger, J. von Berg, A. Franz, and C. Lorenz, "Deep learning based rib centerline extraction and labeling," in *Proc. Int. Workshop Comput. Methods Clin. Appl. Musculoskeletal Imag. (MICCAI)*. Cham, Switzerland: Springer, 2018, pp. 99–113.
- [65] J. Yang et al., Mar. 2020, "Rib fracture detection and classification challenge," doi: [10.5281/zenodo.3715934](https://doi.org/10.5281/zenodo.3715934).
- [66] K. He, G. Gkioxari, P. Dollár, and R. Girshick, "Mask R-CNN," *IEEE Trans. Pattern Anal. Mach. Intell.*, vol. 42, no. 2, pp. 386–397, Feb. 2020.
- [67] K. Sun, B. Xiao, D. Liu, and J. Wang, "Deep high-resolution representation learning for human pose estimation," in *Proc. IEEE/CVF Conf. Comput. Vis. Pattern Recognit. (CVPR)*, Jun. 2019, pp. 5686–5696.
- [68] F. I. Diakogiannis, F. Waldner, P. Caccetta, and C. Wu, "ResUNet-a: A deep learning framework for semantic segmentation of remotely sensed data," *ISPRS J. Photogramm. Remote Sens.*, vol. 162, pp. 94–114, Apr. 2020.
- [69] O. Ronneberger, P. Fischer, and T. Brox, "U-Net: Convolutional networks for biomedical image segmentation," in *Proc. 18th Int. Conf. Med. Image Comput. Comput.-Assist. Intervent.*, 2015, pp. 234–241.
- [70] R. C. Contributors, Feb. 2024, "Challenge solutions of the RibFrac challenge" [10.5281/zenodo.10658441](https://doi.org/10.5281/zenodo.10658441).
- [71] S. Chen, K. Ma, and Y. Zheng, "Med3D: Transfer learning for 3D medical image analysis," 2019, *arXiv:1904.00625*.
- [72] P. Wang et al., "Understanding convolution for semantic segmentation," in *Proc. IEEE Winter Conf. Appl. Comput. Vis. (WACV)*, Mar. 2018, pp. 1451–1460.
- [73] Z. Tu and X. Bai, "Auto-context and its application to high-level vision tasks and 3D brain image segmentation," *IEEE Trans. Pattern Anal. Mach. Intell.*, vol. 32, no. 10, pp. 1744–1757, Oct. 2010.
- [74] H. Tang, C. Zhang, and X. Xie, "Nodulenet: Decoupled false positive reduction for pulmonary nodule detection and segmentation," in *Proc. 22nd Int. Conf. Med. Image Comput. Comput.-Assist. Intervent.*, D. Shen et al., Ed., 2019, pp. 266–274.
- [75] J. Hu, L. Shen, and G. Sun, "Squeeze-and-Excitation networks," in *Proc. IEEE/CVF Conf. Comput. Vis. Pattern Recognit.*, Jun. 2018, pp. 7132–7141.
- [76] F. Isensee, P. F. Jaeger, S. A. A. Kohl, J. Petersen, and K. H. Maier-Hein, "nnU-Net: A self-configuring method for deep learning-based biomedical image segmentation," *Nature Methods*, vol. 18, no. 2, pp. 203–211, Feb. 2021.
- [77] Z. Liu, H. Tang, Y. Lin, and S. Han, "Point-voxel CNN for efficient 3D deep learning," in *Proc. Adv. Neural Inf. Process. Syst.*, vol. 32, 2019, pp. 1–11.
- [78] M. Moor et al., "Foundation models for generalist medical artificial intelligence," *Nature*, vol. 616, no. 7956, pp. 259–265, Apr. 2023.
- [79] J. Yang, H. B. Li, and D. Wei, "The impact of ChatGPT and LLMs on medical imaging stakeholders: Perspectives and use cases," *Meta-Radiol.*, vol. 1, no. 1, Jun. 2023, Art. no. 100007.
- [80] J. Wasserthal et al., "TotalSegmentator: Robust segmentation of 104 anatomic structures in CT images," *Radiology: Artif. Intell.*, vol. 5, no. 5, pp. 1–18, Sep. 2023.
- [81] C. R. Qi, Y. Li, H. Su, and L. Guibas, "PointNet++: Deep hierarchical feature learning on point sets in a metric space," in *Proc. Adv. Neural Inf. Process. Syst.*, Jan. 2017, pp. 5105–5114.
- [82] J. Long, E. Shelhamer, and T. Darrell, "Fully convolutional networks for semantic segmentation," in *Proc. IEEE Conf. Comput. Vis. Pattern Recognit. (CVPR)*, Jun. 2015, pp. 3431–3440.
- [83] L.-C. Chen, Y. Zhu, G. Papandreou, F. Schroff, and H. Adam, "Encoder-decoder with atrous separable convolution for semantic image segmentation," in *Proc. Eur. Conf. Comput. Vis. (ECCV)*, 2018, pp. 801–818.
- [84] F. Isensee et al., "nnU-Net revisited: A call for rigorous validation in 3D medical image segmentation," in *Proc. Int. Conf. Med. Image Comput. Comput.-Assist. Intervent.* Cham, Switzerland: Springer, 2024, pp. 488–498.
- [85] J. Yang et al., "Medmnist v2-a large-scale lightweight benchmark for 2D and 3D biomedical image classification," *Sci. Data*, vol. 10, no. 1, p. 41, 2023.
- [86] L. Maier-Hein et al., "Why rankings of biomedical image analysis competitions should be interpreted with care," *Nat. Commun.*, vol. 9, no. 1, p. 5217, 2018.
- [87] L. Maier-Hein et al., "BIAS: Transparent reporting of biomedical image analysis challenges," *Med. Image Anal.*, vol. 66, Dec. 2020, Art. no. 101796.
- [88] M. Wiesenfarth et al., "Methods and open-source toolkit for analyzing and visualizing challenge results," *Sci. Rep.*, vol. 11, no. 1, p. 2369, Jan. 2021.
- [89] A. Dosovitskiy et al., "An image is worth 16×16 words: Transformers for image recognition at scale," 2020, *arXiv:2010.11929*.
- [90] T.-Y. Lin, P. Dollár, R. Girshick, K. He, B. Hariharan, and S. Belongie, "Feature pyramid networks for object detection," in *Proc. IEEE Conf. Comput. Vis. Pattern Recognit. (CVPR)*, Jul. 2017, pp. 936–944.
- [91] K. Simonyan and A. Zisserman, "Very deep convolutional networks for large-scale image recognition," 2014, *arXiv:1409.1556*.
- [92] K. Lee, J. Zung, P. Li, V. Jain, and H. S. Seung, "Superhuman accuracy on the snemi3D connectomics challenge," 2017, *arXiv:1706.00120*.
- [93] W. R. Crum, O. Camara, and D. L. G. Hill, "Generalized overlap measures for evaluation and validation in medical image analysis," *IEEE Trans. Med. Imag.*, vol. 25, no. 11, pp. 1451–1461, Nov. 2006.
- [94] C. H. Sudre, W. Li, T. Vercauteren, S. Ourselin, and M. J. Cardoso, "Generalised dice overlap as a deep learning loss function for highly unbalanced segmentations," in *Proc. 7th Int. Workshop Deep Learn. Med. Image Anal., Int. Workshop Multimodal Learn. Clin. Decis. Support*. Cham, Switzerland: Springer, Sep. 2017, pp. 240–248.
- [95] S. S. M. Salehi, D. Erdogmus, and A. Gholipour, "Tversky loss function for image segmentation using 3D fully convolutional deep networks," in *Machine Learning in Medical Imaging*, Q. Wang, Y. Shi, H.-I. Suk, and K. Suzuki, Eds., Cham, Switzerland: Springer, 2017, pp. 379–387.
- [96] K. Kamnitsas et al., "Efficient multi-scale 3D CNN with fully connected CRF for accurate brain lesion segmentation," *Med. Image Anal.*, vol. 36, pp. 61–78, Feb. 2017.